Monte Carlo simulations of X-ray absorption in the interstellar medium

Diploma Thesis in Physics

submitted by

Wiebke Eikmann

Advisor: Prof. Dr. Jörn Wilms

Dr. Karl Remeis Observatory Bamberg, Astronomical Institute of the

Friedrich-Alexander-University of Erlangen-Nürnberg

May 31, 2012

Abstract

Although prior measurements of X-ray radiation from the sun exist, the first detection of a cosmical X-ray source in 1962 was still a surprise. It turned out that the signal cames from the binary system Scorpius X-1. Still a long time after this discovery, the physical process leading to the observed luminosities was mysterious. Several years later, the idea that the radiation originates from mass accretion onto a compact object, for example, a neutron star or a black hole, became general accepted. This is the case in X-ray binaries: they consist of a compact object and a normal star orbiting around their common center of mass. If the compact object orbits close to its companion star, mass accretion becomes possible. The systems are often deep embedded in sourrounding interstellar medium. As the photons interact with the particles via scattering and photo-ionization, the primary spectrum is significantly modified after it has passed the medium. In this thesis, a Monte Carlo simulation of radiative transfer in the interstellar medium is presented. After the basic idea behind the Monte Carlo method is described in the introduction, the physical background of the involved process are outlined in chapter 2. The general algorithm is described in detail in chapter 3, with special emphasis on the used Monte Carlo technique. The shape of the resulting spectra is strongly dependent on the extension and properties of the interstellar medium. Therefore, in chapter 4, spectra are shown produced within different geometries. The results are compared with prior models. The shape and intensity of the fluorescence lines is an important diagnostic tool to determine the properties of the interstellar medium around X-ray sources. For this reason, different parameters characterizing the iron K_α-line are calculated as a function of degree of absorption, viewing angle and iron abundance. The resulting values may help to interpret observational data.

Zusammenfassung

Obwohl schon im Jahr 1949 Röntgenstrahlung von der Sonne detektiert wurde, war die Entdeckung der ersten kosmischen Röntgenquelle 1962, das Doppelsternsystem Scorpius-X-1, eine Überraschung. Zunächst war unklar, welche physikalischen Prozesse für die intensive Strahlung im Röntgenbereich verantwortlich sein könnten. In den folgenden Jahren setzte sich dann die Vorstellung durch, dass die Strahlung durch die Akretion von Materie auf ein kompaktes Objekt, zum Beispiel auf einen Neutronenstern oder ein schwarzes Loch, entsteht. Denkbare Konstellationen für dieses Szenario sind beispielsweise Röntgendoppelsternsysteme, in denen ein kompaktes Objekt und ein Hauptreihenstern um ihren gemeinsamen Schwerpunkt kreisen. Ist der Orbit eng genug, wird Materietransfer von dem Begleitstern auf das kompakte Objekt möglich. In der unmittelbaren Umgebung solcher Systeme befinden sich häufig große Mengen Gas, das die Röntgenquelle auch komplett umhüllen kann. Beim Durchgang der Strahlung wird das Spektrum durch die Wechselwirkung zwischen den Photonen und den Teilchen im Medium modifiziert und verändert sich. Die wichtigsten Prozesse sind hier Compton Streuung und Photoabsorption, sowie das Auftreten von Fluoreszenzlinien. In dieser Arbeit wird eine Monte Carlo Simulation vorgestellt, die den Strahlungstransport durch interstellares Medium nachbildet und so absorbierte Spektren berechnet. Nachmdem in der Einleitung kurz die Idee hinter der Monte Carlo Methode erklärt wird, wird in Kapitel 2 zunächst kurz auf die physikalischen Grundlagen dieser Simulation eingegangen, inwieweit sie für das Verständniss dieser Arbeit wichtig sind. Anschließend wird in Kapitel 3 der der Simulation zugrunde liegende Algorithmus vorgestellt und die wichtigsten Routinen im einzelnen erklärt. Die Form der absorbierten Spektren hängt sehr von der Verteilung und der Lage des interstellaren Mediums im Bezug auf die Quelle ab, was in Kapitel 4 anhand verschiedener Geometrien gezeigt wird. Die Spektren werden zudem noch mit bereits vorhandenen Modelen verglichen. Intensität und Form der Fluorezenzlinien verändern sich ebenfalls mit der Beschaffenheit des Mediums und sind daher wichtige Hilfsmittel, um die Eigenschaften von dem die Quelle umgebenden Material zu bestimmen. In Kapitel 5 werden daher verschiedene Parameter der Eisen K_α-Linie in Abhängigkeit von Absorptionsgrad, Blickrichtung und Eisenhäufigkeit untersucht. Der Verlauf und die Größenordnung der so erhaltenen Werte könnte für die Interpretation von Beobachtungsdaten hilfreich sein.

Contents

List of Figures

1 From the simple to the sublime: The Monte Carlo method

The first thought cross your mind when reading "Monte Carlo" may related with casinos and playing poker. In fact, this gives you an excellent hint where this method came from. Games of chance have been fascinating men for a long time ago and still do. Already the old Romans were playing dice and today many people spend their time and money sitting in gambling houses. A game of chance is strongly affected by any kind of randomizing process and that may account for its attraction. Even if a player is very skilled in a special game, he could just get a bad break and loose. To handle this randomness, it becomes interesting to estimate the probability of success and losing. The first way to manage that is straightforward calculating with probability theory. This is certainly the most accurate method and it will provide the exact solution if any exists. On the other hand, the procedure may get very extensive for more complicated problems. Stanislav Ulam, who liked to relax playing solitaire, was one of the developers of the Monte Carlo method and describes the second way in his autobiography "Adventures of a Mathematician" (Ulam, 1976): the idea is to estimate the probability of winning by playing many games of solitaire and then simply count the fraction of games that could be solved. This procedure is rather practical then compute all combinatorial possibilities using probability theory which leads anyway to a solution only for elementary cases. For sufficiently complicated problems, this procedure is preferred to the examination of all probability branches. The result after a quantity of simulated games will not lead to the exact answer, but we can give the degree of accuracy and improve the result by increasing the number of simulated games.

Getting information about a stochastic process by just trying it out many times and considering the statistical outcomes is the basic idea of Monte Carlo method. In their book "Monte Carlo Methods" (Kalos & Whitlock, 2008), M. Kalos and Whitlock define the Monte Carlo Method as the use of random numbers in a calculation that have the structure of a stochastic process. By stochastic process a sequence of states is meant whose evolution is determined by random events. In the solitaire simulation, this random event would be the accidental arrangement of shuffled cards.

A similar procedure can also be used to solve integrals. Monte Carlo integration is a numerical integration method using random numbers. To estimate a domain A, we put A inside a different domain B whose area can be easily calculated. Then we produce a number N of random points inside B. The area of domain A is thus given by the fraction of points that lie also in A multiplied by the area of domain B. For the mathematical background of Monte Carlo integration, see, for example, Caflisch (1998).

A simple example of use is the approximation of the mathematical constant π as described, for example, by Kalos & Whitlock (2008): considering a circle with radius r and its circumscribed square with side length $2r$. The ratio of the area of the circle $A_\mathrm{C} = \pi r^2$ to the area of the square $A_\mathrm{S} = 4r^2$ is $\pi/4$. To estimate π, we generate N random points inside the square. The ratio between the points inside the circle and the total number of random points will tend to $\pi/4$ for a large number N of simulated points. In Figure 1, the method is demonstrated for 100 random points. The deviation from π was on average about $\sim 5\%$. By increasing the number of random points, the estimation will approximate π.

This method is not the best and fastest way to approximate π, but the example demonstrates the solution of a mathematical problem by random sampling. In this case, the integral

$$I = \int\limits_0^1 \int\limits_0^{\sqrt{1-x^2}} \mathrm{d}x\mathrm{d}y.$$

is estimated. Random sampling is often the computationally most effective method to evalute multidimensional integrals.

Using random numbers to reconstruct stochastic sequences of events has a wide field of application. The simulated systems are usually characterized by a significant uncertainty of the input parameters as well as of its evolution. In social science which strongly relies on statistic methods, hypothesis can be tested with Monte Carlo method as described, for example, by Mooney (1997). It is also used to solve insurance and financial problems (see Glasserman, 2003) like risk estimation. In statistical physics and chemistry, Monte Carlo simulation allows to treat systems where thousands of par-

Figure 1: Illustration of Monte Carlo Integration for $N = 100$ random points.

ticles are involved. Examples of use in physics are heat transfer, simulation of quantum systems and nuclear physics.

In this thesis, a simulation of radiative transfer is presented. This problem is well appropriate to be analyzed by Monte Carlo simulation. As M. Kalos mentioned, the simulation can be seen both as solution of the equations of radiative transfer and as a typical Monte Carlo:

"The emission of radiation from atoms and its interaction with matter is an example of a natural stochastic process since each event is to some degree predictable (...). It lends itself very well to a rather straightforward stochastic simulation. But the average behavior of such radiation can also be described by mathematical equations whose numerical solution can be obtained using Monte Carlo methods. Indeed the same computer code can be viewed simultaneously as a "natural simulation" or as a solution of of the equations by random sampling (Kalos & Whitlock, 2008, p. 3)."

Within the simulation, single photons are conducted step by step through a medium. The propagation is influenced by random events like absorption, emission and scattering. Each process occurs corresponding to a certain probability distribution and is choosed by random numbers. To get a complete spectrum, one has simple to run the simulation over and over again collecting the escaped photons.

This is a good example how Monte Carlo simulation works. A complex stochastic process is split up into its individual components and each of this sub-routines is separately figured out. Information about the entire process is obtained by considering a lot of such sequences.

In this sense Nicholas Metropolis describes the spirit of Monte Carlo method fittingly with the words: "From the simple to the sublime" (Metropolis, 1987, p. 126).

2 Physical background

The Monte Carlo code presented in this thesis is designed to reproduce X-ray spectra observed from real sources. In this chapter, the physical background of the simulation is outlined. I will first give a short overview about cosmical X-ray sources with special emphasis on X-ray binaries, which formation and evolution is explained in more detail. Subsequently, the involved interaction mechanisms between matter and light like Compton scattering and photo-ionization are explained. Finally, the basic equations describing the radiative transfer through a medium are presented.

2.1 X-ray Sources

As long as humans exist, they look at the sky and are fascinated by the stars. It is therefore not surprising that optical astronomy has a long history. Because the eye is naturally only sensitive for *visible* light and of the absence of other detectors, it took a long time until one noticed that astronomical objects emit also light in other wavelengths. Karl Jansky was the first who observed a none optical signal from outside the solar system, it was a radio signal from the center of the Milky Way (Jansky, 1933).
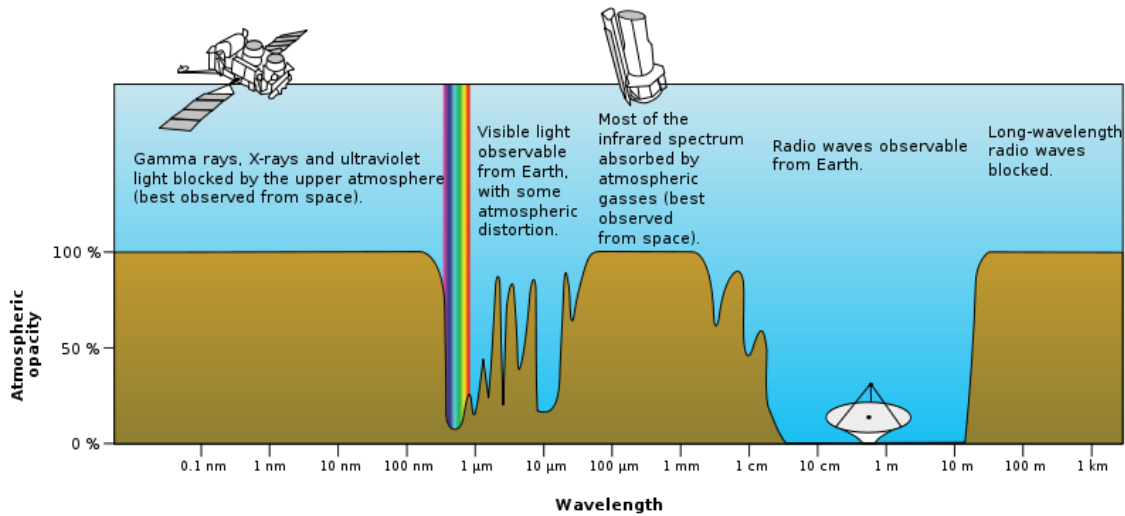
Figure 2: Illustration of Earth's atmosphere opacity for electromagnetic radiation (source: NASA public domain, acquired from Wikimedia Commons)

As seen in Figure 2, only radiation in the optical and radio range is observable from ground, the Earth's atmosphere is opaque beyond the ultraviolet region (Trümper & Murdin, 2000) and hence measurements must be performed in space. The first X-ray measurements from the sun were done by Friedman in 1949 during a rocket flight (Friedman et al., 1951). Despite this descovery, the first observation of an extrasolar X-ray source (Giacconi et al., 1962) in the vicinity of the Scorpius constellation was still a surprise. This source, called Scorpius X-1, has an X-ray luminosity of 2×10^{38} erg s^{-1}. For comparison, the sun has a maximal luminosity of 5×10^{27} erg/s in X-ray[1]. One more time after this discovery, the process that leads to an X-ray emission of such quantity was still mysterious. Zel'Dovich (1964) and Salpeter (1964) were the first who suggest accretion of

---

[1]X-ray luminosities from: http://heasarc.gsfc.nasa.gov/docs/heasarc/headates/brightest.html

9
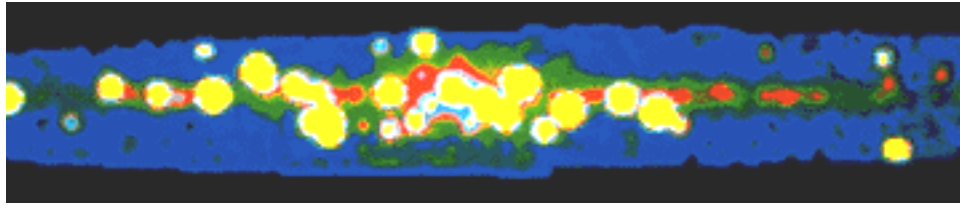
Figure 3: X-ray binaries (yellow points) near the Galactic Center (source: NASA public domain)

matter onto a massive object as a possible energy source. In the following years, this idea became generally accepted.

Figure 3 shows the Galactic center in the X-ray regime. The sky in this energy range is dominated by a few hundred very bright stars and most of these stars would be X-ray binaries.[2]

A X-ray binary is a system consisting of a normal star, which still produces energy by nuclear fusion, and a stellar remnant like a neutron star or a black hole. The compact object and the companion star are gravitanionally bound and rotate around their common center of mass. The compact object has about the same mass as our sun but with a radius of only $\sim 10\,\text{km}$. Thus, it is extremely dense. Material is drawn from the companion star and falls onto the compact object by realizing X-rays.[3]

In the following, an outline of the circumstances that lead to the formation of such a system is given. Beginning with the evolution of a single star whose life may end with the genesis of a compact object, the evolution of binary systems is described. Depending on the parameters of the system, different accretion mechanisms are possible, which are explained at last.

2.1.1 Stellar evolution

The evolution of a single star is elementary for understanding the formation and mechanisms in binary systems. The process of stellar evolution is very complex and many details are still under discussion. Therefore, I will give only a rough overview about this subject and summarize the most basic facts. For details see, e.g. ,Kippenhahn & Weigert (1990) or Salaris & Cassisi (2005).

In 1911, E. Hertzsprung and H. Rosenberg and later in 1914 also H. Russell developed a diagram, today known as Hertzsprung-Russel Diagram (HRD), that illustrates the relation between the spectral and other characteristics of stars. In a modern HRD, the absolute magnitude or luminosity of the stars is plotted against their spectral type which is equivalent to an effective temperature. Traditionally, the coordinate axes are chosen such that the cool and dim stars are located at right bottom and the bright and hot stars at top left. In Figure 4 (a), a HRD of stars in the vicinity of the sun is shown.

It is remarkable that stars are not uniformly distributed over the whole diagram, but are mainly concentrated at the *main sequence*, extending from the top left corner to the bottom right corner. But not all stars can be found in this narrow sequence, some stars has moved above the main sequence (bright but cool) while also few stars can be found below. This motion in HRD is due to the stellar evolution. The star is born by starting hydrogen burning and, depending on its initial mass, settles on the mean sequence where it will spent most of its lifetime. When the star is already

---

[2]after: `http://imagine.gsfc.nasa.gov/docs/science/know_l2/binaries.html`
[3]after: `http://heasarc.gsfc.nasa.gov/docs/binary.html`
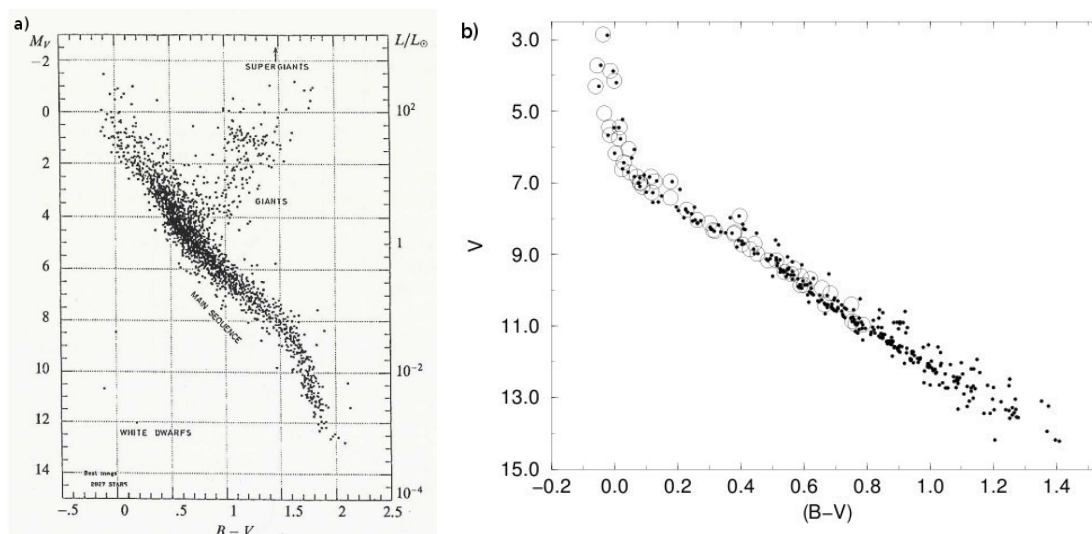
Figure 4: a) Hertzsprung-Russell diagram for stars in the vicinity of the sun (from Lindegren, 1992). Not all stars are located in the main sequence, some have developed to red giants and a few to white dwarfs. b) HRD of the young star cluster Pleiades (from Hansen-Ruiz & van Leeuwen, 1997). In this diagram, all stars can still be found in the main sequence.

older and further evolved, it will leave the main sequence to enter the red-giant phase and finally die remaining a compact object. The motion in the HRD for stars with different initial masses is, for example, described by Weigert et al. (2005). For comparison, the HRD of the young stellar cluster Pleiades in Figure 4 (b) has no developed stars.

Star formation   It is established that star formation in our Galaxy occurs in dense molecular clouds which containe a substantial fraction of the total mass of the interstellar medium (Zuckerman & Palmer, 1974). As described in detail by McKee & Ostriker (2007), star formation is initialized by turbulences in the cloud which may cause a local collapse: due to velocity fluctuations in the warm and diffuse medium, matter can be pushed into thermal unstable regions where the gas cools down by forming a denser domain. This clumps attract even more gas and collapse at some point.

The density and temperature in the core increases and at a certain point hydrogen burning becomes possible. In this thermonuclear reaction, several lighter nuclei fuse into one heavier element. Crucial for the energy account is that the nuclei together have a slightly higher mass before the reaction than the resulting nucleus. According to Einstein's equation $E = mc^2$, the missing mass is transformed into energy. By starting hydrogen burning, the collapsing gas cloud has turned into a *star* and will settle on the main sequence according to its mass.

Main sequence   The time a star will remain on the main sequence depends on the supply of hydrogen in its core. This lifetime is proportional to fM/L, where fM is the fraction of the stellar mass M, which is available for nuclear burning, and L is the averaged luminosity. Since luminosity and mass are strongly correlated, a heavier star will spent less time on main sequence than a lighter one.[4]

---

[4]after: http://map.gsfc.nasa.gov/universe/rel_stars.html

The nuclear fusion of hydrogen into helium can run in two different cycles, the *pp*-chain and the *CNO*-cycle, which are explained in the following. In both cycles the net result is given by

$$^4H \rightarrow {}^4He.$$
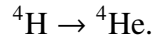
For clarity, second products are not shown in the following reactions. The chemical equations can be found, for example, in Salaris & Cassisi, p. 118f (2005).
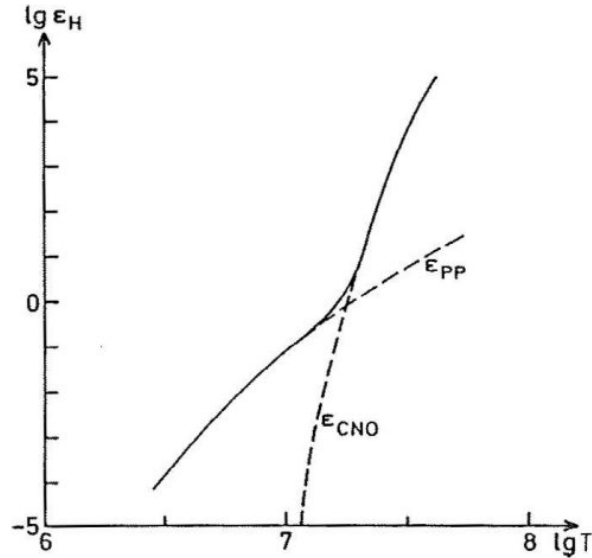
Figure 5: Temperature-dependence of the pp-chain and the CNO-cycle (from Salaris & Cassisi, 2005, Fig. 18.8).

- **Proton-Proton chain**
  For a moderate core temperature, helium is produced by the proton-proton chain:

  $$^1H + {}^1H \rightarrow {}^2D$$
  $$^2D + {}^1H \rightarrow {}^3He$$
  $$^3He + {}^3He \rightarrow {}^4He + 2{}^1H$$
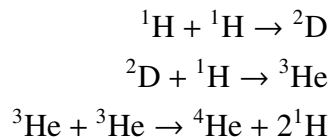
  This process is called pp-I cycle. Also a pp-II and pp-III cycle exist, but pp-I dominates.

- **CNO-cycle**
  In the cycle, the presence of some isotopes of C, N or O are necessary:

  $$^{12}C + {}^1H \rightarrow {}^{13}N$$
  $$^{13}N \rightarrow {}^{13}C$$
  $$^{13}C + {}^1H \rightarrow {}^{14}N$$
  $$^{14}N + {}^1H \rightarrow {}^{15}O$$
  $$^{15}O \rightarrow {}^{15}N$$
  $$^{15}N + {}^1H \rightarrow {}^{12}C + {}^4He$$
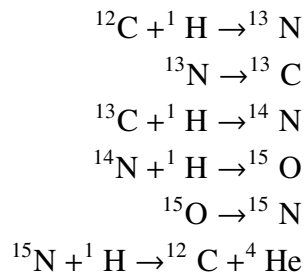
  Since C, N and O are both produced and destroyed, they behave like catalyzer in this cycle.

The rate of energy production ε is temperature dependent as explained, for example, by Rolfs & Rodney (1988), p. 375.: since at lower stellar temperatures the pp-chain is mainly responsible for the energy production (see also Fig. 5), the CNO-cycle becomes more important for higher temperatures and is finally the dominating process. The steep rise of ε_{CNO} is mainly caused by the high Coulomb barriers occurring in the CNO reactions. In the pp-chain, two protons collide which means the Coulomb potential must be overcome. This is easier for a singly charged proton than for the reactions in the CNO cycle (see Salpeter 1955).

In Salaris & Cassisi (2005) the efficiency of nuclear energy production as a function of the temperature $\varepsilon \propto T^{\upsilon}$ is specified for the different cycles. For a core temperature $T \leq 15 \times 10^6$ K, the pp-chain process dominates with an averaged $\upsilon \approx 4$. The CNO cycle becomes important for higher temperatures where $\varepsilon_{CNO} \propto T^{18}$ at $T \approx 10 \times 10^6$ K. The comparison between the energy productions rates from pp-chain and CNO-cycle leads to the conclusion that hydrogen is faster exhausted in high massive stars, which reach higher temperatures.

Higher burning stages   If all hydrogen in the central region of a star is converted into helium, the temperature is too low to start helium burning an thus the nuclear burning expires at first. By the decrease of radiation pressure, the star contracts by its own weight resulting in a density and temperature increase in the core. If it is heavy enough, the temperature and pressure reach critical values to ignite the next burning stage. In addition, further burning areas exist in shells around the core where the temperature is high enough to convert lighter elements. Due to this *shell-burning*, the radiation pressure increase in the outer layers and the star expands. In this phase, the star is called a red giant. At this principle, the star passes several subsequent burning stages, which lifetime decreases consequently.

The last burning stage is the nuclear fusion of silicon into iron. Since iron is the nucleus with the highest binding energy, the fusion into a next heavier element would require additional energy to stabilize the core instead of an energy gain. Therefore the star collapses, if the silicon in the core is exhausted. The different burning stages and evolutionary steps are explained in detail, for example, by Salaris & Cassisi (2005).

Stellar remnants   After a star has burned all its resources, it evolves into one of three types of objects, depending on its initial mass.

- **White draws**
  The gravitational collapse of the burned star stopps when the core reaches a critical density, wherein the electron gas becomes degenerated. The pressure of the degenerated electron gas can resist the gravitational pressure as long as the mass is below ~ 1.4 M$_\odot$ (the Chandrasekhar limit, see Chandrasekhar, 1931). Since stars with masses > 2 M$_\odot$ loose a large part of their envelope before the collapse (see Weidemann et al., 1992), stars with masses up to $\sim 8 - 10$ M$_\odot$ ends up as *withe dwarfs* (from Weigert et al., 2005, p. 202).

- **Neutron stars**
  For stars of higher initial masses $\sim 11 - 25$ M$_\odot$ (Salaris & Cassisi 2005, p. 233), the pressure of the degenerated electron gas can not stop the collapse. The core is further compressed and the electrons are "pressed" into the protons. The infalling matter hits the core that is no more compressible and bounces back. Strong shock fronts are formed and the star explodes

as a *supernova*. The envelope is ejected and a *neutron star* is left. The neutron concentrate a mass of ~ 1.4 M$_\odot$ in a radius of just 10 km and has a density $\rho \approx 1 \times 10^{14}$ g/cm^3 (Srinivasan, 1997).

- **Black holes**
  If the the remnant of the supernova exceeds a mass limit of ~ 2.5 M$_\odot$ (corresponding to an initial progenitor mass above ~ 25 M$_\odot$) the pressure of the degenerated neutrons cannot stabilize the collapse and the core will shrink to a *black hole* (see Salaris & Cassisi, 2005, p. 236). Its gravitational field is so strong that even light and any other forms of energy cannot escape from it. This is equivalent to the speed of light c is smaller than the escape velocity v_{esc} needed to escape from a gravitational field generated by a mass M of radius R:

$$v_{esc}^2 = 2\frac{GM}{R} > c^2.$$

This relation gives the radius

$$R_S = 2\frac{GM}{c^2} = 2.95 \times 10^5 \frac{M}{M_\odot}$$

also called the *Schwarzschild radius* for which the escape velocity for a test mass becomes greater than c.

2.1.2 Evolution of binary systems

During the collapse of a gas cloud is usually more than a single star formed, thus it is not unlikely that two stars are born nearby. Due to gravity, the two stars may bound together and start to rotate around a common center of mass. The gravitational potential of such a bound system is more complicated than for a single mass. This problem, also known as *three-body-problem*, can described in an idealized version by the *Roche potential* (for a detailed derivation see, for example, Frank et al., 2002), where the stars are considered as point masses. Assuming a co-rotating reference frame, where the masses M_1, M_2 located at the positions $\mathbf{r}_1$, $\mathbf{r}_2$ are fixed. The gravitational field, experienced by a test particle at position $\mathbf{r}$ with the mass $m \ll M_1, M_2$, is than given by

$$\Phi(\mathbf{r}) = -\frac{GM_1}{|\mathbf{r} - \mathbf{r}_1|} - \frac{GM_2}{|\mathbf{r} - \mathbf{r}_2|} - \frac{1}{2}(\Omega \times \mathbf{r})^2.$$

The first two terms describe the gravitational potential of M_1, M_2, respectively, the last term is the centrifugal force. Due to the co-rotating frame of reference where the position vectors of the stars $\mathbf{r}_1$, $\mathbf{r}_2$ are fixed, the angular momentum Ω is fixed as well. In Figure 6, the equipotential surfaces of the Roche potential for stars with mass ratio $M_1/M_2 = 0.6$ is plotted.

The innermost surface connected by Lagrange point L_1 is called the *Roche surface* and represents the maximal size of the stars. Exceeds one star its *Roche volume*, the matter outside the Roche surface is no longer bound and can drift away or is accreted by the other star.

For a detailed overview about the evolution of binary systems see, for example, van den Heuvel (2011). The evolution of the individual stars in a binary system follows the steps explained in section 2.1.1 and the massive star will evolute faster than its lighter companion. Therefore, it may happen that the heavier star ends up as a white dwarf while the other star is still on the main
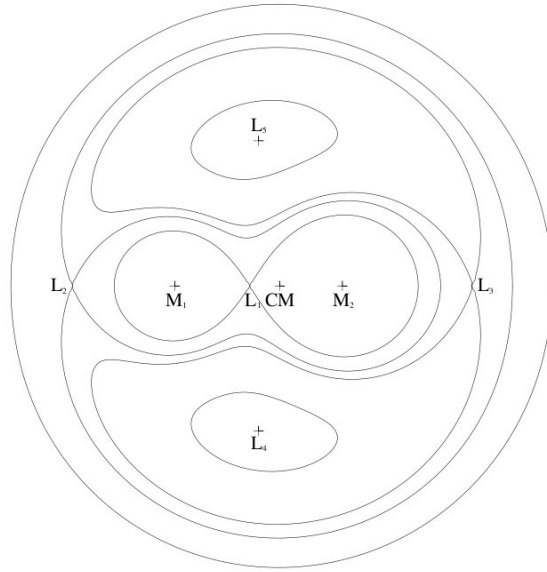
Figure 6: The equipotential surfaces of the Roche potential calculated for a mass ratio $M_1/M_2 = 0.6$. The five Lagrange points ($L_1, ..., L_5$) and the center of mass (CM) are also marked.

sequence. The companion star further evolves and enters at any time the red-giant phase accompanied by extension of its outer layers. The white dwarf may become able to accrete matter from its companion and once its mass exceeds the Chandrasekhar limit, the star explodes in a supernova remaining a neutron star or a black hole.

2.1.3 Accretion mechanism

If, for some reason, mass is transferred from the companion star onto the compact object, the energy gained by moving a test particle with mass m from infinity onto the surface of an object with mass M and radius R is given by

$$\Delta E = \frac{GMm}{R}.$$

The energy will released in X-ray radiation. Dependent on the parameters of the binary system, several accretion mechanism are possible, which are explained in the following.

Roche Lobe Overflow   Since in many cases the companion star is a expanded star in the *red-giant phase*. Once it exceeds its Roche volume, the outer layers are no longer bound and

Figure 7: Artistic impression of the high-mass X-ray binary system. The outer layer from the companion star is stripped off and reaches the compact object via Roche Lobe Overflow (source: NASA public domain).

the plasma from the star's atmosphere passes through L_1 into the Roche volume of the compact

object. This accretion mechanism is called *Roche Lobe overflow*. Due to the rotation of the donor star, the captured material has angular momentum and does not fall directly onto the compact object. Instead, an accretion disk is formed, where the matter moves on spiral trajectories in direction to the central mass. In Figure 7, an artistic impression of such a system is shown. The plasma flows from the companion star onto the compact object by forming an accretion disk.

Wind Accretion   Since the stellar wind of normal stars is usually weak, for O- or B-type stars the mass loss rate due to stellar wind can be up to $\dot{M}_{\mathrm{wind}} = 1 \times 10^{-6} - 1 \times 10^{-4} \ \mathrm{M}_\odot \mathrm{yr}^{-1}$. In a typical binary system, the compact object is orbiting around its companion star in a distance of less than a stellar radius and therefore it is deep embedded in the wind. Due to an angular momentum, an accretion disk or an accretion stream may be formed. Wind accretion does not imply a constant accretion rate leading to a uniform X-ray luminosity. The high-mass X-ray binary Vela X-1 shows, for example, significant flares of more than 3.0 Crab between $20 - 60$ keV since the averaged flux is around 250 mCrab. One possible explanation might be the clumps in the wind (Fürst et al., 2010).
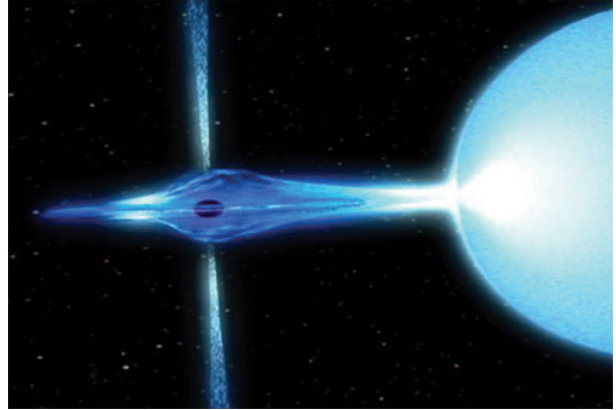
Figure 8: Artwork of a compact object that accretes from the stellar wind of an OB giant companion (source: NASA).

Be-accretion   In these binaries, the companion star is a Be-star. A Be-star is a B-type star that exhibits emission lines over its spectrum. This spectral component is attributed to a circumstellar gaseous environment. Due to the fast rotation of the Be-star, an equatorial disk may be formed (for a detailed discussion of Be-stars, see, for example, Porter & Rivinius, 2003).
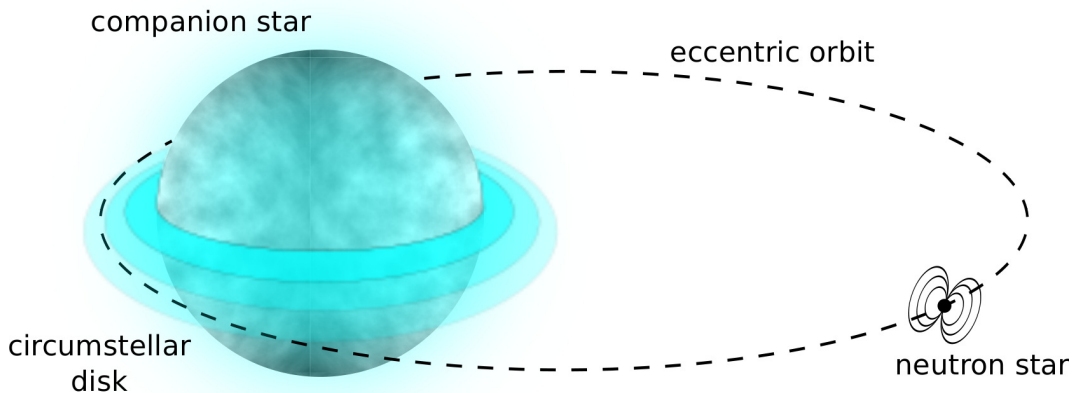
Figure 9: A neutron star orbiting around a Be-star in an eccentric orbit. When the compact object enters the disk, mass accretion becomes possible and X-ray flares can be observed (priv. com. M. Kühnel).

Mass accretion is possible if the compact object passes the circumstellar envelope during its periastron passage. The accretion disk of the neutron star or black hole is filled and an X-ray outburst can be observed. As a result of the previous supernova explosion, the orbits of most binary systems are high eccentric. Once the compact object is leaving the periastron, the accretion rate decreases rapidly due to lack of mass. When an accretion disk was formed, the compact object can maintain accretion for a time but shortly after the periastron passage, the X-ray source will become fainter and by approaching the apastron, the X-ray luminosity decreases in most cases below any detectable limit. In Figure 9, the orbit of such a system is shown. This kind of X-ray sources are also called *transient sources*.

2.2 Interaction between radiation and matter

A photon can be understood as a particle with zero mass and zero charge traveling always with c, the speed of light. Being electrically neutral, photons do not constantly loose energy due to Compton interaction as charged particles do, but travel a certain distance before they undergo a more significant process. Below a photon energy of $\sim 10\,\text{keV}$ photo-ionization is the dominant effect (see Fig. 10).
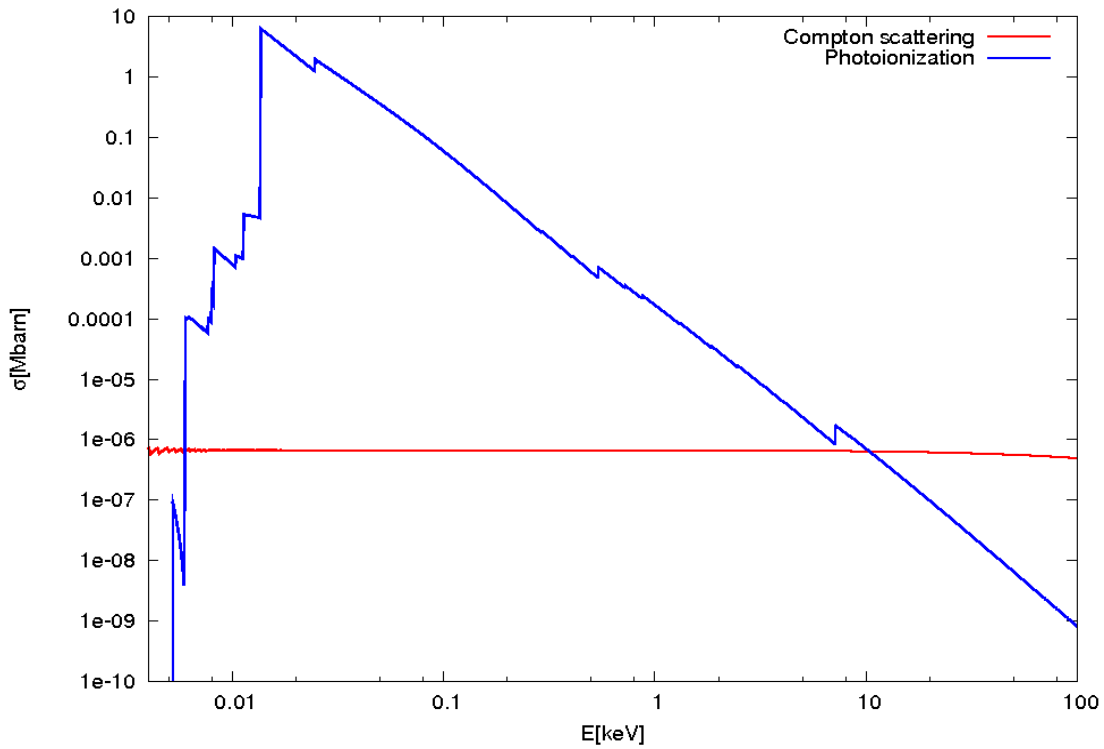
Figure 10: Photo-ionization cross-section and Klein-Nishina cross-section for Compton scattering per hydrogen atom. As seen, photo-ionization is the dominant process for photons with energies up to 10 keV. Elemental abundances are those given by Wilms et al. (2000). For the fit parameters which are used to calculate the photo-ionization cross-section see Verner & Yakovlev (1995).

In this process the photon is absorbed removing an inner-shell electron from an atom or ion which takes the photon energy away. The vacancy left by the kicked-out electron may be filled with

an outer-shell electron by emitting either a photon which has an energy characteristical for this transition or by ejecting an Auger electron. The further process is called *fluorescence*.

Above 10 keV the photon is usually Compton scattered. Depending on the electron temperature the photon either looses energy and heats the medium or it is up-scattered by hot electrons. If the photon energy is at least 2 $m_e c^2$, pair production is also possible.

In this chapter, I will give a short overview of the physical background of Compton scattering (section 2.2.1) and photo-ionization (section 2.2.2) including the related process of fluorescence (section 2.2.3).

2.2.1 Compton scattering

Compton scattering is a type of inelastic scattering that photons experience in matter. This process causes a shift in the photon's energy, which is called Compton effect. It was first observed and published in 1923 by A. Compton.

This change in energy can only be understood in terms of Quantum Mechanics. In the low energy limit the scattering process reduces to elastic Thomson scattering which is the low energy approximation of Compton scattering and can be described classically. Thomson scattering explains the elastic scattering of radiation by free charged particles using classical electromagnetism (after Rybicki & Lightman, 1986).

In this approach the scattered photon does not change its energy

$$E = E'$$

and the differential cross-section for Thomson scattering is given by

$$\frac{d\sigma_T}{d\Omega} = \frac{1}{2} r_0^2 (1 + \cos^2 \alpha) \qquad (1)$$

where $r_0 = c^2/mc^2$ gives a magnitude scale of the point charge (for electrons, r_0 means the classical electron radius) and α is the angle between the incident and the scattered photon (see Fig. 11). The differential cross-section is proportional to m^{-2}, thus scattering with electrons as the least massive free charged particles is dominating. For example, the cross-section for scattering on protons is reduced by a factor $\left(m_e/m_p\right)^2 \approx 10^{-7}$, therefore scattering on heavier particles is not an issue. Integrating over the solid angle Ω we get the total Thomson cross-section

Figure 11: Compton scattering

$$\sigma_T = \frac{8\pi}{3} r_0^2. \qquad (2)$$

For an electron this expression results in 6.652×10^{-25} cm^{-2} = 0.665 barn .

For increasing photon energies the classical approach of Thomson scattering is no longer valid. Is a X-ray or γ-ray photon scattered by an electron, Quantum effects have an influence on the scattering event in two ways (Rybicki & Lightman, 1986):

- The photon will experience an energy shift due to the recoil of the charge.
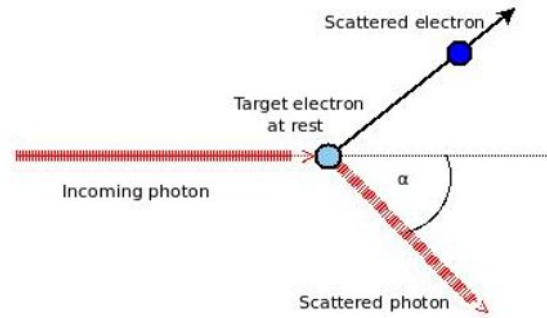
- The classical Thomson cross-section has to be modified

The following derivations mainly refer to Pozdnyakov et al. (1983). Treating the photon with frequency f as a particle with energy $E = hf$, it has a well defined momentum $\mathbf{p} = (hf/c)\,\mathbf{\Omega}$. Assume it is scattered by an electron of energy γmc^2 and momentum $\mathbf{p} = \gamma m\mathbf{v}$ with velocity vector $\mathbf{v}$ and $\gamma = (1 - v^2/c^2)^{-1/2}$. Prior to the scattering event, the photon and electron four momenta are given respectively by

$$\mathbf{p}_4 = (\mathbf{p}, i\gamma mc), \quad \mathbf{k}_4 = \left(\frac{hf\mathbf{\Omega}}{c}, \frac{ihf}{c} \right)$$

Considering energy and momentum conservation, the sum of photon and electron four momentum does not change during the interaction

$$\mathbf{p}_4 + \mathbf{k}_4 = \mathbf{p}'_4 + \mathbf{k}'_4$$

where $\mathbf{p}'_4$ and $\mathbf{k}'_4$ denotes the four momenta after the scattering event. Defining $\mu = \mathbf{\Omega v}/c$, $\mu' = \mathbf{\Omega'v'}/c$ and the scattering angle $\alpha = \cos^{-1}(\mathbf{\Omega} \cdot \mathbf{\Omega'})$ (see Fig. 11) and after some conversions, the comparative frequency shift is given by

$$\frac{f'}{f} = \frac{1 - \frac{\mu v}{c}}{1 - \frac{\mu' v}{c} + \frac{hf}{\gamma mc^2}(1 - \cos\alpha)}. \tag{3}$$

If the target electron is at rest ($|\mathbf{v}| = 0$), Eq. (3) is reduced to

$$\frac{f'}{f} = \frac{1}{1 + \frac{hf}{mc^2}(1 - \cos\alpha)}. \tag{4}$$

This equation can be written as

$$\lambda' - \lambda = \lambda_C (1 - \cos\alpha)$$

where λ and λ' are the wavelengths of the photon prior and after the collision, respectively. The constant $\lambda_C = h/(mc)$ is called Compton wavelength and constitutes 2.42631×10^{-12} m for an electron.

If, in contrast, the electron traveling at high speed, the relativistic Doppler effect becomes more important. To get the frequency shift for a photon with frequency f in the observer's frame, it has to be considered that from the electron's point of view, the photon appears redshifted with

$$f_0 = \gamma f \left(1 - \frac{\mu v}{c} \right). \tag{5}$$

If $hf_0 \ll mc^2$ in the electron's reference frame, the low-energy approximation of Thomson scattering is again valid and the collision is assumed to be elastic $f_0 \approx f'$. Back in the observer's frame, the frequency of the scattered photon is given by

$$f' = \frac{f'_0}{\gamma \left(1 - \frac{\mu' v}{c} \right)} \approx \frac{f_0}{\gamma \left(1 - \frac{\mu' v}{c} \right)} = f \frac{\left(1 - \frac{\mu v}{c} \right)}{\left(1 - \frac{\mu' v}{c} \right)}.$$

For low-frequency photons the relativistic Doppler effect will dominate the energy shift of the photon.
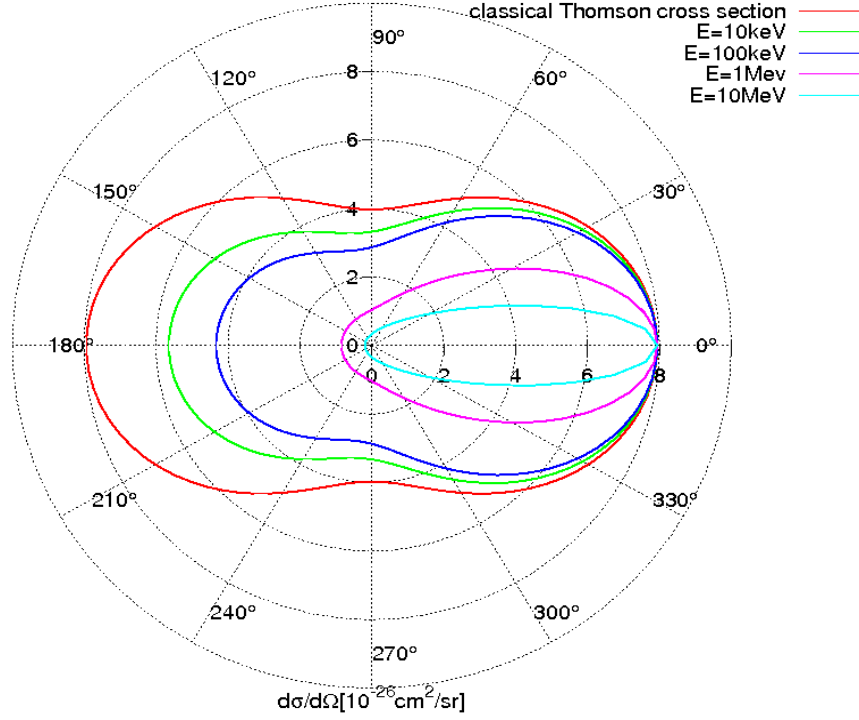
Figure 12: Differential Klein-Nishina cross section

In t 1928, O. Klein and Y. Nishina derived the differential quantum mechanic cross-section for Compton scattering with free electrons at rest:

$$\frac{d\sigma_C}{d\Omega} = \frac{3}{16\pi}\sigma_T \left(\frac{f'}{f}\right)^2 \left[\left(\frac{f}{f'}\right) + \left(\frac{f'}{f}\right) - \sin^2\alpha\right]. \tag{6}$$

With $x = hf / (m_e c^2)$ and considering Eq. 4, Eq. 6 can be written as

$$\frac{d\sigma_C}{d\Omega} = \frac{3}{8\pi}\sigma_T \left(\frac{1 + \cos^2\alpha}{2}\right)\left(\frac{1}{1 + x(1 - \cos\alpha)}\right)^2 \left[1 + \frac{x^2(1 - \cos\alpha)^2}{(1 + \cos^2\alpha)(1 + x(1 - \cos\alpha))}\right]. \tag{7}$$

In Fig. 12, this quantum mechanic differential cross-section is displayed. For comparison, the classical Thomson cross-section is also shown. As expected, the cross-section approximates Thomson scattering for low photon energies. In this classical regime, the probability of being scattered in a certain direction is symmetric around $\alpha = 90°$. With increasing energy back-scattering occurs more and more rarely, while the possibility of scattering forward remains constant. This fact plays an important role in shaping line profiles as discussed in chapter 5.

Integrating Eq. 7 over the solid angle $d\Omega$, we finally get the total quantum mechanical cross-section

$$\sigma_C = \sigma_T \frac{3}{4}\left\{\frac{1 + x}{x^3}\left[\frac{2x(1 + x)}{1 + 2x} - \ln(1 + 2x)\right] + \frac{1}{2x}\ln(1 + 2x) - \frac{1 + 3x}{(1 + 2x)^2}\right\}. \tag{8}$$

This equation is called the Klein-Nishina formula.

2.2.2 Photo-ionization

Photo-ionization describes the process in which a photon removes one or more electrons from the absorbing atom or ion. This effect is also known as *Photo-effect*. An incident photon with energy hf impacts an atom X and depending on whether the photon energy is high enough, a bound electron may be kicked out leaving an ionized atom and an additional charge (after Kaastra & Mewe, 1993):

$$hf + X = X^+ + e.$$

The ejected photo-electron carries away an energy E_e equal to the difference between the photon energy and the binding energy E_{ion} of the removed electron:

$$E_e = \frac{1}{2}m_e v^2 = hf - E_{ion}.$$

Since the bound electron is lifted to an upper state which lies in the continuum, this process is also called *bound-free transition*. The transition probability is related to the photo-ionaization cross-section which depends on the energy of the incident photon and the kind of the target atom. Each individual electron subshell accounts for the overall cross-section and its contributions change with ionization stage. Cross-section measurements exist for neutral atoms but are still very scarce for multiply charged ions (Champeaux et al., 2003). As analytical calculations are possible only for hydrogen-like ions, it is necessary to resort to numerical methods. Before I outline the method how the photo-ionization cross-sections are achieved in the simulation, I will first roughly describe the configuration and denotation of the electron shell and its subshells.

Electron shell An electron shell can be thought as a defined residence space for electrons around a nucleus. Expressed in simplified terms the shells are arranged from inside to out and the outer shells are only occupied if the inner ones are already filled with electrons. The basic construction of the electron shells is, for example, explained by Demtröder (2006):

The electron shell is related to the principal quantum number $n \geq 1$ and for each value of it there are n possible values for the azimuthal quantum number $l = 0, 1, 2, ..., n-1$. This results in

$$\sum_{l=0}^{n-1} (2l + 1) = n^2$$

different states per shell and each of them can be occupied with a pair of electrons with opposite spin. An electron shell with principal quantum number n thus can hold at most $2n^2$ electrons.

In table 1, the first 4 electron shells and their subshells are shown additionally to their respective maximal occupation number. In the simulation presented in this thesis, elements are included up to an atomic number of $Z = 30$. Therefore, the highest shell we have to consider is the $4s$ subshell.

Cross-sections The differential cross section of bound-free transitions from a state with principal quantum number n and subshell l for a photon with energy E is given by (see Rybicki & Lightman, 1986)

$$\sigma_{bf}(E) = \frac{512\pi^7 m_e e^{10} Z^4}{3\sqrt{3}ch^6 n^5} \frac{g(\omega, n, l, Z)}{\omega^3} = \frac{64\pi^4 m_e e^{10} Z^4}{3\sqrt{3}ch^3 n^5} \frac{g(E, n, l, Z)}{E^3} = \sigma_{bf,c} g(E, n, l, Z) \qquad (9)$$

n (shell name)	l (name sub shell)	max. electrons per sub shell	max. electrons per shell
1 (K-shell)	0 (1s)	2	2
2 (L-shell)	0 (2s)	2	8
	1 (2p)	6	
3 (M-shell)	0 (3s)	2	18
	1 (3p)	6	
	2 (3d)	10	
4 (N-shell)	0 (4s)	2	32
	1 (4p)	6	
	2 (4d)	10	
	3 (4f)	14	

Table 1: Notation and number of electrons for each shell up to $n = 4$

where Z is the atomic number, $e = 1.60 \times 10^{-19}$ C the elementary charge, $m_e = 9.10 \times 10^{-31}$ kg the electron mass, $h = 6.63 \times 10^{-34}$ Js Planck's constant, $c = 2.99 \times 10^8$ ms^{-1} the speed of light in vacuum and $\omega = 2\pi f = 2\pi E/h$ the angular frequency of the photon.[5]

Eq. 9 is only valid for a photon energy exceeding the binding energy E_{Th} of subshell nl, otherwise $\sigma_{bf} = 0$ as the photon energy is not enough to eject an electron. The factor $g(E, n, l, Z)$ is called *Gaunt-factor* and summarizes the quantum mechanical corrections since $\sigma_{bf,c}$ is the semi-classical cross-section for photo-absorption.

Karzas & Latter (1961) calculated the Gaunt factor for atoms which are ionized so far that they only have a single electron and the computation can be done by considering a pure Coulomb field. The result of these calculation is that the Gaunt-factor is ~ 1 for photon energies close to the binding energy of the particular shell and decreases with increasing photon energy. Therefore the quantum mechanical cross-section is smaller for high energies than the semi-classical approach.

As the photo-absorption cross-section for a single shell is zero if $E < E_{Th}$ while it is maximal close to the binding energy, absorption edges are visible where the cross-section increases abruptly when absorption from the next higher shell becomes possible.

Verner & Yakovlev (1995) present a set of photo-ionization cross-sections for the ground state shells of all atoms and ions for $Z \leqq 30$. The partial cross section $\sigma_{nl}(E)$ for a subshell nl is described by the fitting formula

$$\sigma_{nl}(E) = \sigma_0 F\left(\frac{E}{E_0}\right)$$

with

$$F(y) = \left[(y-1)^2 + y_w^2\right] y^{-Q} \left(1 + \sqrt{(y/y_a)}\right)^{-P}$$

where $y = E/E_0$ and y_w, y_a, σ_0, E_0 and P are the fit parameters and $Q = 5.5 + l - 0.5P$. By summarizing the partial cross-sections

$$\sigma_{Z,I}(E) = \sum_{n,l} \sigma_{n,l}(E)$$

---

[5]values of physical constants from `http://physics.nist.gov/cuu/Constants/`

the overall absorptivity for an atom or ion can be calculated. If the ionization structure and the elemental abundances of the absorbing material is known, the overall photo-ionization cross-section is given by

$$\sigma_{\text{tot}}(E) = \sum_{Z,I} a_Z \sigma_{Z,I}(E)$$

where a_Z is the number of atoms with proton number Z per hydrogen atom.

In Figure 13, the partial cross-sections for the M-shell ($n = 3$) of neutral iron calculated after Verner & Yakovlev (1995) are plotted as an example.
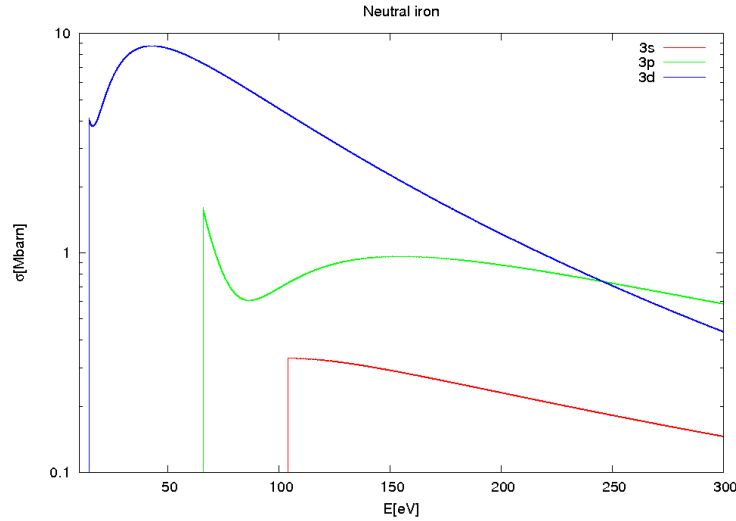
Figure 13: Partial cross-section for the M-shell of neutral iron.

For the innermost subshell $3s$ the cross-section is the smallest during the ionization energy is the largest and for $E \gg E_{\text{Th}}$ the cross-section decreases. For the outer shells, interaction with the field caused by the other shell electrons becomes important. The minima, evident in the plots for subshell $3p$ and $3d$ result from this interaction (see Wilms, 1996, and references therein).

2.2.3 Auger ionization and Fluorescence

Once an inner-shell electron is removed, the vacancy will be filled subsequently by electron cascades from higher shells (Kaastra & Mewe, 1993). The energy difference is compensated either by a radiative transition called *fluorescence* or by the emission of an *Auger-electron*. In Figure 14 the different processes are sketched.

Various transition rates are possible and the resulting number of photons and electrons emitted during the cascade is given by a probability distribution. If Auger processes are involved, a single vacancy can lead to a highly ionized atom. The description of the individual processes below follows Kaastra & Mewe (1993) and Bambynek et al. (1972).

- **Fluorescence**
  A vacancy in a shell X may be filled by a radiative transition from a higher shell Y. The difference between the binding energies E_x, E_y of the respective shells is emitted as fluorescence photon with an energy

  $$E_{\text{ph}} = E_x - E_y.$$

Figure 14: Skatch of the different options after the absorption of a photon by an inner shell: (a) fluorescence with emission of a characteristic X-ray photon, (b) Coster-Kronig transition followed by fluorescence and (c) the emission of an Auger electron (graphic from Wilms, 1996).
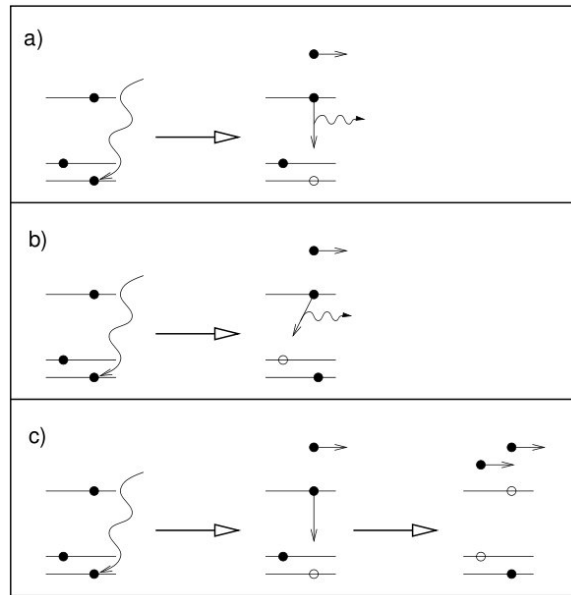
As the line energy is specific for a certain transition the absorbing element can be identified by the fluorescence line. Since the transitions in ions show a slightly different line energy the ionization state can also be determined. Fluorescence and Auger ionization may occur both for the same initial vacancy and therefore the probability that during the cascade a specific line photon is emitted is in general less than one. This probability is expressed in the *fluorescence yield Y* which is defined as the number of emitted line photons per ionization (Kaastra & Mewe, 1993).

- **Auger ionization**
  The alternative option to fill the initial vacancy in shell X is a radiationless Auger transition XYZ. An electron from shell $Y > X$ takes the place left by the knocked out electron by ejecting another electron from subshell $Z \geq Y$. The energy of the Auger electron is given by

$$E_{\text{Auger}} = E_X - E_Y - E_Z.$$

- **Coster-Kronig transition**
  If shell X and Y have both the same principal quantum number, the transition is called a Coster-Kronig transition.

In the simulation, the Auger effect is considered by reducing the probability that a photon is re-emitted after being absorbed as fluorescence photon.

2.3 Absorption of X-rays in the interstellar medium

When a beam of photons passes through matter, various events are possible. As discussed above, Compton scattering and photo-ionization occur. There is also a certain probability that no inter-

action occurs and the photon escapes. This probability increases with decreasing density of target particles. In the following, the general equations that describe the radiative transfer in medium are outlined. As the absorption is strongly dependent on the elemental composition of the medium, the abundances used in this simulation are presented.

2.3.1 General equations

The derivations below follows mainly Rybicki & Lightman (1986). When a ray of light travels a distance ds through absorbing material, the intensity I_f at frequency f can be described by the following equation:

$$dI_f = -\alpha_f I_f ds \tag{10}$$

where α_f in units of cm^{-1} is the absorption coefficient for a photon with energy $E = hf$. This phenomenological law can be written as

$$dI_f = -n\sigma_f I_f ds = -\frac{1}{\lambda_f} I_f ds \tag{11}$$

where n represents the particle density (number of particles per unit volume) and σ_f the cross-section for a photon with frequency f. The parameter λ_f is called the *mean free path* and it denotes the average distance a photon can travel without being scattered or absorbed.

The fraction of photons that is escaping from the medium without interaction is then given by

$$\frac{I_f(s)}{I_f(s_0)} = \exp\left[-\int_{s_0}^{s} \frac{1}{\lambda_f(s')} ds'\right]. \tag{12}$$

Integrated over a distance s we get:

$$\frac{I_f}{I_{f,0}} = e^{-\frac{s}{\lambda_f}} = e^{-\tau} \tag{13}$$

where τ is the optical depth.

In astronomy, the amount of matter between source and observer is usually described by the *hydrogen column density* N_H which is defined as the number of hydrogen atoms in the line of sight per unit area. The real number of particles is thus given by considering all elemental abundances respective to hydrogen.

2.3.2 Abundances

The photo-absorption cross-section σ_f and the amount of particles along the line of sight is dependent on the considered elemental mixture of the absorbing medium.

For the main part of the spectra simulated in this thesis, the elemental abundances for interstellar medium presented by Wilms et al. (2000) were used and I point also to this paper for further details. Prior calculations were done, for example, by Morrison & McCammon (1983). The abundances listed in table 2 are normalized to a hydrogen abundance of $\log A_H = 12$ (Wilms et al., 2000).

Element	Z	$12 + \log A_Z$
H	1	12.00
He	2	10.99
C	6	8.38
N	7	7.88
O	8	6.69
Ne	10	7.94
Na	11	6.16
Mg	12	7.40
Al	13	6.33
Si	14	7.27
P	15	5.42
S	16	7.09
Cl	17	5.12
Ar	18	6.41
Ca	20	6.20
Ti	22	4.81
Cr	24	5.51
Mn	25	5.34
Fe	26	7.43
Co	27	4.92
Ni	28	6.05

Table 2: Elemental abundances for interstellar medium from Wilms et al. (2000) for the abundant elements

3   Monte-Carlo simulation of radiative transfer

The code presented in this thesis is a Monte Carlo simulation of photon transport in the interstellar medium. The original code was implemented by J. Wilms (1996) and further developed by L.Barragán. For a general introduction in Monte Carlo methods see, for example, Deak (1990) or, with special emphasis on the simulation of X-ray spectra, Pozdnyakov et al. (1983).

The simulation is designed to exploring the modification a X-ray spectrum expiriences by passing through the interstellar medium. A photon emitted by an astronomical source hits a cloud arranged in a certain geometry and defined by density, temperature and elemental abundances. The photon may interact with the atoms and ions within the medium. It will change its direction and energy if it collides with an electron and or it is absorbed by photo-ionization (see Section 2.2.1). As described in Section 2.2.2 and 2.2.3, a line photon with an energy specific for each element can be emitted if absorption takes place. In addition, there is a possibility that the photon escapes without any interaction. According to its composition and other characteristics, the medium modifies the shape of the input spectrum significantly.

Similar simulations are done for example by Matt et al. (1991) to model radiation from an accretion disk with special emphasis on the Fe K_α-line and the high energy bump at $10 - 50$ keV and by Odaka et al. (2011a) which gives a very detailed overview also about the framework of the

used Monte Carlo simulation.

To simulate the transport of photons through a medium, the involved probability distributions have to be identified and defined. Methods are needed to sample values from these distributions by random numbers. The interactions itself and the associated modification of the photon's properties have to be modeled. In addition, the geometry has to be modeled including algorithms to determine whether a photon can assumed to be still in medium.

In this chapter, I will first give an overview of the general algorithm. Additionally, the method of weights is explained, a way to improve the statistics by splitting a process in its different probability branches. Subsequently, the different parts of the program including the used Monte Carlo techniques are discussed in detail.

This chapter basically refers to the thesis of Wilms (1996) and the corresponding documentation (Wilms, 2002). Most of the algorithms and derivations are adopted from there. Please refer to this papers for further details and references.

3.1   General Algorithm and the method of photon splitting

In Figure 15 the basic algorithm used in this thesis is shown (after Wilms, 2002). In the following, I will go step by step through the individual program sequences and I will explain the main parts shortly.

1. A photon defined by its position $\mathbf{r} = (x, y, z)$, direction $\mathbf{d} = (d_x, d_y, d_z)$, energy E and weight w (the meaning of this parameter is explained below) is generated at source's coordinates and propagated through the medium.

2. A random path length x is sampled using to the probability distribution $I/I_0 = \exp(-x/\lambda)$ (see Eq. 13). Then the photon is propagated by x.

3. Now we test if the photon is still in the medium. If it is, the photon has interacted with an electron or atom and we continue with step 4. Elsewise, we bin the escaped photon in a spectrum and go back to step 1.

4. The type of interaction, absorption or Compton scattering, is calculated by weighting their respective cross-sections. In the case the photon is absorbed, we continue with step 5, otherwise with step 6.

5. The photon has removed an inner shell electron. At first, the absorbing element and the shell have to be figured out. Considering the different fluorescence yields, we determine the shell from which the vacancy is filled and whether the energy is carried away by an Auger electron or a line photon. If an Auger electron is ejected, the photon is destroyed. In case of line emission, we change the photon energy according to the specific line and sample its direction from an isotropic distribution.

6. The photon is Compton scattered of a quasi-free electron. The scattering angle is sampled using the differential Klein-Nishina formula eq. 7 and the new direction and energy (see eq. 4) of the scattered photon is calculated .
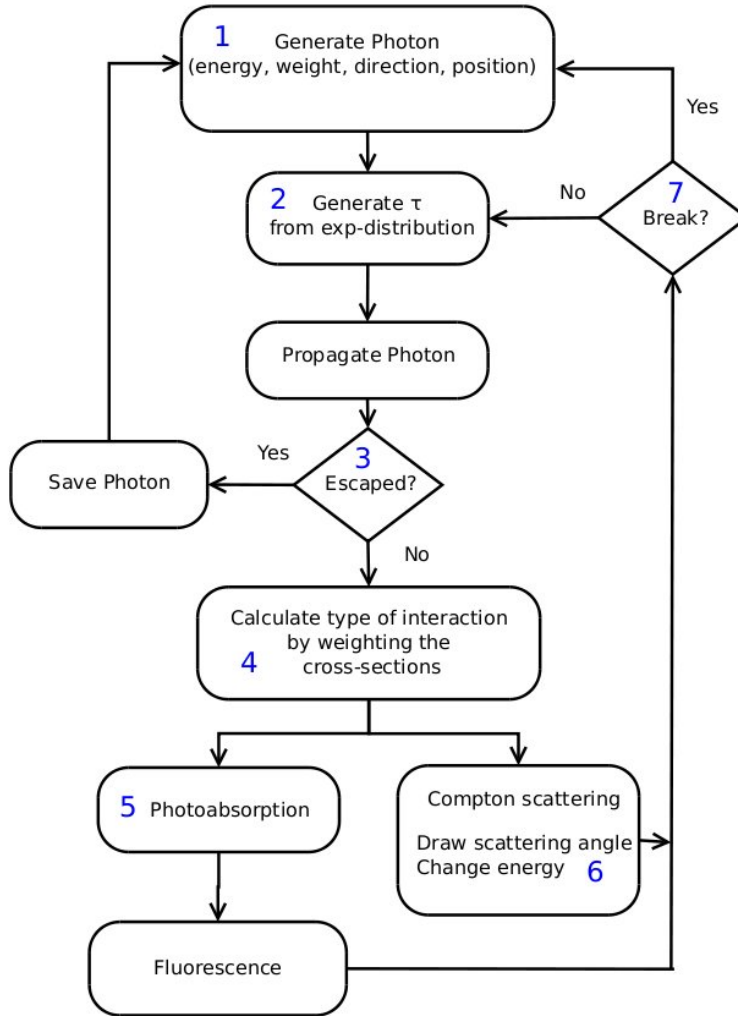
Figure 15: General algorithm of radiative transfer simulated by the Monte Carlo method

7. We test, if it makes any sense to continue propagating the photon or if we could consider it absorbed due to its low energy. When the photon gets absorbed, we go back to step 1, else wise we continue with step 2.

In step 1, each photon is assigned a weight w. This means, we do not necessarily consider a single photon ($w = 1$) but also fractional parts ($w < 1$) of it as well as photon packets with $w > 1$. This method was firstly described by Pozdnyakov et al. (1983) and I refer to this paper for the mathematical details.

In this way, the energies of the generated photons can be modeled. To simulate the radiation of a cosmical source, the weights of the input photons are assigned according to teh soruce's spectral distribution which is usually described by a powerlaw

$$N(E) = N_0 E^{-\alpha} \tag{14}$$

where α is the dimensionless photon index and N_0 a normalization constant in units of keV^{-1}cm^{-2}s^{-1}. If the overall input spectrum covers an energy range from $E_{\min}$ to $E_{\max}$, the generated photon will have an energy E_x with $E_{\min} \leq E_x \leq E_{\max}$. To ensure that the entire spectrum is power law distributed, we assign the weight of the photon to

$$w_x = \frac{E_x^{-\alpha}}{\int_{E_{\min}}^{E_{\max}} N(E)\mathrm{d}E}.$$

A higher weighting corresponds to a higher probability that a photon with energy E_x is emitted from the source. In the simulation, we generate the same number of photons in each energy interval but weighten them differently.

As one can easily imagine, a large part of the photons (particularly in the low energy range and for an optically thick medium) is absorbed and only a few photons escape the medium. This makes the method inefficient, in the way that many photons are needed to obtain a meaningful spectrum which in turn leads to a high computational effort.

A method to handle this problem is the introduction of *escape-weights* also known as "photon splitting technique", as described, for example, by Odaka et al. (2011b): first, the fraction of photons that escape the medium without scattering is calculated. Subsequently that part of the photon package is propagated outside the medium towards its original direction. The rest of the photon is scattered considering the equations in Section 2.2.1. We are also no longer forced to make a decision, but can split the photon and trace the various probability branches.

In Figure 16, a trace of such a such a splitting process is shown for an input photon with an energy of 100 keV.

The photon emitted at $z = 1$ is moving downwards and hits the plan, which is infinitely extended in the minus Z-direction at $z = 0$. After entering the cloud the photon is scattered around until its energy or weight is low enough to satisfy the abortion's criterion. The solid line represents the fraction of the photon, that always remains in the medium while the dashed lines symbolize the part that escapes. The weight decreases the longer the photon is in the medium. By adding a minimum weight to the abortion's criterion, we set up to which probability the photon is still propagated. If the photon moves towards the medium's edge, there is a probability to escape and the photon will split. Especially in the semi-infinite slab geometry (described in Sec. 3.4.2), where only the back-scattered photons are of interest, the technique of photon-splitting is important. As back-scattering is rare for high photon energies there would be a lot of run-time without escaping weights.

This way, we gain information from each simulated photon path which significantly improves the statistics. In Figure 17, a Compton shoulder of the Fe K$_\alpha$-line, simulated with and without using photon-splitting. Especially the left part of the Compton shoulder is much better resolved.

The method of weights can also be used to model fluorescence, especially if we are only interested in particular lines. Assuming, for example, the Fe K$_\alpha$-line is of special interest and we would like to gain information about it each time a photon is emitted via fluorescence. The probability that the photon removes an electron from K-shell of neutral iron is given by $P_{\mathrm{Fe,K}} = \sigma_{\mathrm{Fe,K}}/\sigma_{\mathrm{tot}}$ where $\sigma_{\mathrm{Fe,K}}$ is the partial cross-section of the K-shell of neutral iron and σ_{total} is the total photo-absorption cross-section including all shells and elements. First, we stipulate that the photon is always absorbed by the K-shell of neutral iron and multiply its weight with $P_{\mathrm{Fe,K}}$. Subsequently, we change the photon´s energy to the Fe K$_\alpha$-line energy and reduce once again its weight by the total fluorescence yield (see chapter 2.2.3). Since only the weight counts for the output spectrum,
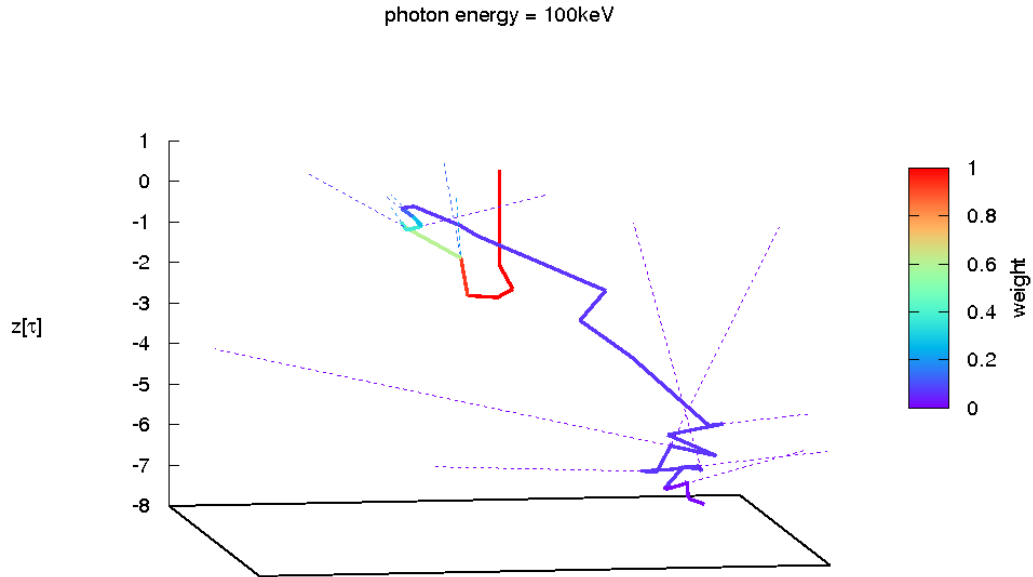
Figure 16: A photon trace calculated with escape-weights in a semi-infinite flat geometry. The dashed lines represent the escaping part of the photon.

each fluorescence photon gives statistical informations about the iron lines by conserving the actual emission probability.

3.2   Random numbers

The basic idea of Monte Carlo simulation is to model events by chance and therefore a good random number generator is of crucial importance. Random numbers used in a computer simulation should meet the following requirements (Wilms, 1996):

1. The output of a computer is based on an algorithm and therefore it is of course deterministic. In hardware random number generators, additional devices like a clock or a γ-ray counter are used to receive random numbers. Otherwise one needs an algorithm that computes values which have the same properties as random numbers. The values achieved in this way are also called *pseudo random numbers*. Since a periodicity in the used values would lead to wrong outcomes, the sequences may not be repeated during the simulation.

2. In order to replicate certain random events of interest and for reasons of bug-fixing, the generated random sequences should be reproducible. Therefore the generators based on any external randomizing device are not suitable.

3. The random number generator is called many millions times during a simulation and therefore it is necessary that the algorithm used is very fast.
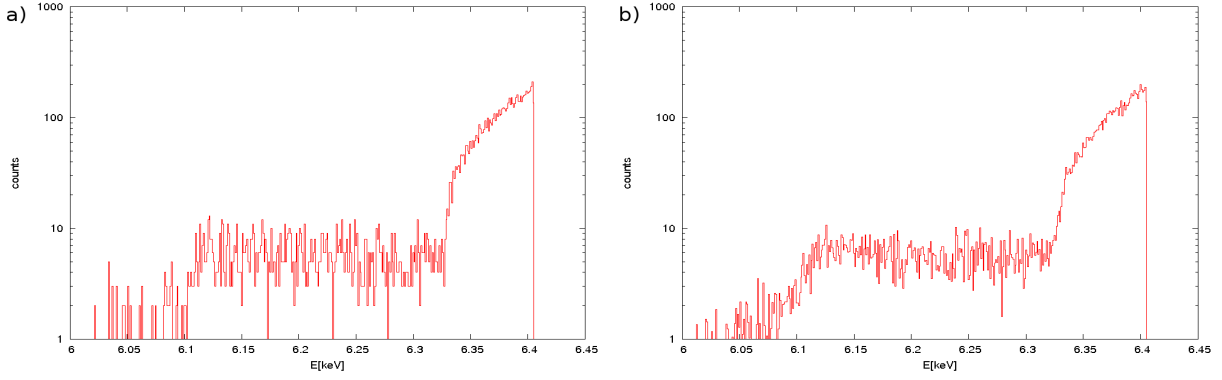
Figure 17: Compton shoulder of the Fe K$_\alpha$-line for a semi-infinite slab geometry, simulated without weights (a) and with weights (b) each for $N = 1 \times 10^4$ input photons.

3.2.1 Uniformly distributed random numbers

To model more complex distributions or events, one uses *ordinary random numbers* uniformly distributed on the interval $[0, 1]$. Most of the algorithms used totay produce such ordinary random number sequences based on the multiplicative congruential method, also called method of residues (Wilms, 1996). In this technique, sequences of integers are generated by the relation

$$x_{i+1} = kx_i + c \, \mathrm{mod}(m)$$

where $i = 0, 1, 2, ...$ and x_0 is the seed value and k, c, m are integers with $x_0, k, c > m$. The *modulus* $c \, \mathrm{mod}(m)$ is the remainder left when c is divided by m. If $c = 0$ the method is called *multiplicative*, otherwise *mixed*. The random number is than given by the sequence $\{x_i/m\}$. The modulus m is often given in the form $m = 2^N$. This expression can easily be evaluated on binary systems. By a suitable choice of the parameters x_0, k, c and m a long sequence of random numbers can be generated without any periodicity (Downham & Roberts, 1967).

An obvious possibility to increase the cycle of independent numbers is to combine different generators. This is the case for the algorithm invented by Wichmann & Hill (1982) which is used in this simulation: it is a combination of three simple multiplicative congruential generators, each with a prime number for the modulus and a simple root for the multiplier. The three results are added and the fractional part is returned.

In Figure 18, the output of Wichmann's generator (1) is compared to a simple multiplicative congruential generator (2), described by Pozdnyakov et al. (1983). Hundred thousand random numbers are produced on the in-

Figure 18: Output of two different random generators: combined generator (1) and a simple multiplicative congruential generator (2)

terval $[0, 1]$ and collected in a grid with a bin-width of $1/100$. Statistically, the number of random values in each bin should be ~ 1000. One can easily see, the output of the combined algorithm varies less around the mean value.
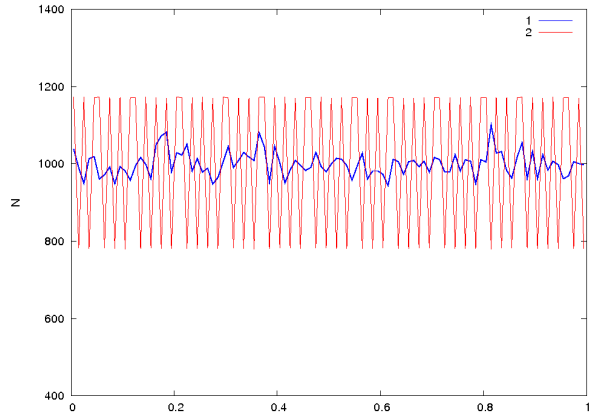
3.2.2 Arbitrarily distributed random sequences

Random variables are given through their distribution function (after Deak 1990, p. 13 ff): Consider a random variable ξ defined on the elementary events ω_i. The probability that a particular random variable $\xi = \xi(\omega_i)$ falls into the interval $[a, b]$ is given by

$$P\{\xi \in [a, b]\} = P\{\cup\omega_i \mid \xi(\omega_i) \in [a, b]\}.$$

If the intersection of any elementary events is empty which implies that only a single event can occure at the same time, than

$$P\left(\bigcup_{i=1}^{\infty} \omega_i\right) = \sum_{i=1}^{\infty} P(\omega_i)$$

and it is sufficient to characterize the variable ξ by probabilities in the form $P\{\xi \in [-\infty, x]\}$. That can also be expressed as

$$P\{\xi < x\} = F(x).$$

$F(x)$ is called the distribution function of the random variable ξ. If

$$F(x) = \int_{-\infty}^{x} f(z)dz$$

is valid for all x, the random variable is called absolutely continuous and $f(x)$ is its density function.

The methods presented below will show how one can generate arbitrarily distributed random variables from ordinary random variables $\xi_n \in [0, 1]$.

The method of inverse functions   This method, here described after Pozdnyakov et al. (1983), can be considered as the standard procedure to obtain specially distributed random variables: Assuming the required values have a distribution function $y = F(x)$ and we can determinate its inverse function to $x = G(y)$. Than the function $\eta = G(\xi)$ will return random variables with distribution function $F(x)$:

$$P\{\eta \leq x\} = P\{G(\xi) \leq x\} = P\{\xi \leq F(x)\} = F(x)$$

This technique is used to model a random path length (step 2 in Fig. 15). Once in the mdium, the photon will travel a certain distance before it is stopped. The free path l is a random variable with the distribution function

$$P\{l \leq x\} = \exp(-x/\lambda)$$

where λ denotes the mean free path (see Section 2.3). The inverse function of $\xi = \exp(-l/\lambda)$ is easily calculated to $l = -\lambda \ln(1 - \xi)$. This last expression can be simplified to

$$l = -\lambda \ln(\xi)$$

since ξ and $(1 - \xi)$ are equally distributed. Suppose the photon is still located a distance L away from the medium's edge with respect to its moving direction. We consider only the part of the photon that remains in medium. Thus, we want to generate a path length $l < L$. The escape

probability is given by $P_{\text{esc}} = \exp\left(-L/\lambda\right)$ since the photon is stopped with probability $P_{\text{in}} = 1 - P_{\text{esc}}$. In this case, the required path length is calculated with

$$l = -\lambda \ln\left(\xi P_{\text{in}}\right).$$

With the method of inverse functions, also random variables can be modeled which distribution is descrete (see Pozdnyakov et al., 1983). Suppose a random variable η can take any of a finite or infinite set of values $x_1, ..., x_m, ...$ each with a respective probability $p_m = P\left\{\eta = x_m\right\}$ and $\sum_m p_m = 1$. Thus, the relation $\eta = G(\xi)$ will lead to

$$
\begin{aligned}
\eta &= x_1 \quad \text{if} \quad \xi < p_1 \\
\eta &= x_2 \quad \text{if} \quad \xi < p_1 + p_2 \\
\eta &= x_3 \quad \text{if} \quad p_1 + p_2 \leq \xi < p_1 + p_2 + p_3
\end{aligned}
\tag{15}
$$

...

To simulate photo-absorption (step 5 in Fig. 15), the absorbing element is chosen by this technique. The overall photo-absorption cross-section σ_{tot} is given by the sum over all partial cross-sections of the individual elements Z, weighted by their respective abundance a_Z. Therefore the equation $\sum_Z a_Z \sigma_Z / \sigma_{\text{tot}} = 1$ is hold and the absorbing element is selected after 15.

Rejection technique This method is a very general technique and it enable us to generate random variables from any distribution. The inverse function has not to be identified, only the probability density is needed as Pozdnyakov et al. (1983) described:

Considering we require a random variable η calculated from a m-dimensional function

$$\eta = g(\xi_1, \xi_2, ..., \xi_m) \quad \text{if} \quad (\xi_1, \xi_2, ..., \xi_m) \in A \tag{16}$$

where A is a specific area in the m-dimensional space. To achieve such a value η, we generate a set of ordinary random numbers $(\xi_1, \xi_2, ..., \xi_m)$ and test, if any ξ lies outside region A. If so, we choose another set, otherwise we compute η from Eq. 16. The probability that a set of ξ falls into A

$$\varepsilon = P\left\{(\xi_1, \xi_2, ..., \xi_m)\right\} \in A$$

is called the *efficiency* of the technique.

In Figure 19, any one dimensional probability distribution is plotted from which we want draw random numbers. A density function $f(x)$ is defined on the interval $[a, b]$ and as the function is normalized, $f(x)$ will take a maximal value c within its domain of definition. We generate a set of two random numbers (α_1, α_2) with $\alpha_1 = a + \xi_1 (b - a)$ and $\alpha_2 = \xi_2 c$. As $\xi_1, \xi_2 \in [0, 1]$ implies $\alpha_1 \in [a, b]$ and $\alpha_1 \in [0, c]$. This is repeated until α_1 satisfies the condition $f(\alpha_1) > \alpha_2$. The values α_1 and α_2 can be considered as uniformly distributed points in the rectangle $[a, b] \times [0, c]$. The test criterion accepts only such a pair of (α_1, α_2) that lies also in the area of the integral of $f(x)$. The efficiency of this method is than given by the ratio of the integral to the area of the rectangle

$$\varepsilon = P\left\{\alpha_2 < f(\alpha_2)\right\} = \frac{\int_a^b f(x)dx}{c\left(b - a\right)} \tag{17}$$

If $f(x)$ is normalized on $[a, b]$, Eq. 17 is reduced to $\varepsilon = \frac{1}{c(b-a)}$.

Another application of rejection technique is the generation of randomly distributed unit vectors on a sphere.

Figure 19: An illustration of rejection techniques

Algorithm 1: Points in a sphere (implemented by Wilms, 1996)

```
do{
        x=2.0*random()-1.0;
        y=2.0*random()-1.0;
        z=2.0*random()-1.0;
        d2  =  x*x  +  y*y  +z*z;
}  while(  d2  >  1.0);
d=sqrt(d2);
a=x/d;
b=y/d;
c=z/d;
```

A point with coordinates x, y, z in three dimensional space is generated within a cube C defined by $[-1, +1] \times [-1, +1] \times [-1, +1]$. Subsequently we test, whether the point lies in a sphere with radius $R = 1$. If so, we accept the values and normalize the vector $[x, y, z]$. The efficiency is then given by

$$\varepsilon = P\{(x, y, z) \in C\} = \frac{\frac{4}{3}\pi R^3}{(2R)^3} = \frac{\pi}{6} \approx 50\%$$

Therefore, the algorithm has to be called twice in the average to get an unit vector. A more obvious possibility to obtain such a random direction may be to generate two random angles $\varphi \in [0, 2\pi]$ and $\vartheta \in [0, \pi]$ by calculating $\varphi = 2\pi\xi_1$ and $\vartheta = \pi\xi_2$ with $\xi_1, \xi_2 \in [0, 1]$. The vector is than given by $\mathbf{x} = [\cos(\varphi)\sin(\vartheta), \sin(\varphi)\sin(\vartheta), \cos(\vartheta)]$. The evaluation of the trigonometric functions requires some computational effort since on binary systems the multiplication by 2 in algorithm 1 is simply managed by the addition of 1 to the exponent of the binary number. Therefore the rejection technique is computationally preferable for this problem.

Method of superposition   The presented version of this method follows the description from Pozdnyakov et al. (1983), for a more general derivation, see Deak (1990). Suppose, we require random variables η whose distribution function $F(x)$ can be written as

$$F(x) = \sum_m c_m F_m(x)$$

with constants $c_m > 0$ and $\sum c_m = 1$. The inverse function of $y = F_m(x)$ is denoted by $x = G_m(y)$. Now we define a new random variable α which can take the values $\gamma = 1, 2, ...$ each with
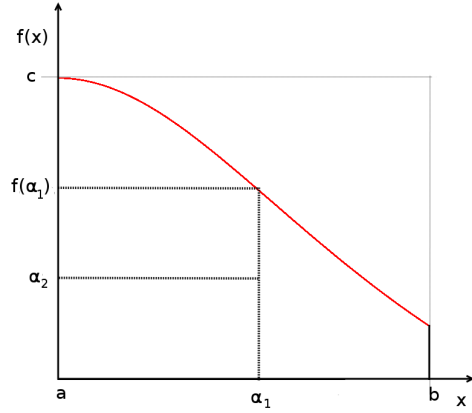
probability $P\{\gamma = m\} = c_m$. To obtain a random number η, we draw two ordinary random numbers $\xi_1, \xi_2 \in [0, 1]$. Using ξ_1, we select a number α. From ξ_2 we get finally the value $\eta = G_\gamma(\xi_2)$, whose distribution function will be $F(x)$:

$$P\{\eta < x\} = \sum_m P\{\eta < x | \gamma = m\}\, P\{\gamma = m\} = \sum_m c_m F_m(x) = F(x).$$

With this technique, the Compton scattering angles α and φ (defined in Fig. 20) can be selected as described by Pozdnyakov et al. (1983):

The angular distribution is given by

$$f(\alpha, \varphi) = \left(\frac{1}{\oint_{4\pi} (d\sigma/d\Omega)\, d\Omega} \right) \frac{d\sigma}{d\Omega}\,(\alpha, \varphi).$$

Since the differential cross-section $(d\sigma/d\Omega)$ is independent of φ, $f(\alpha, \varphi)$ can be written as product of the individual probabilities. For low photon energies, the differential cross-section for Compton scattering is reduced to the Thomson cross-section (Eq. 1). The probability density of the angle φ is $1/(2\pi)$ as scattering in this direction is uniformly. By defining $\mu = \cos(\alpha)$, the distribution for the second angle α is given by

Figure 20: Scattering angles α, φ. The red arrows denotes the direction of rhe photon before and after the scattering.

$$f(\mu) = \frac{3}{8}\left(1 + \mu^2\right) \tag{18}$$

for $-1 < \mu < +1$. As Pozdnyakov et al. (1983) noticed, the inverse method would lead to that the equation $\mu^3 + 3\mu + 4 = 8\xi$ has to be solved for each required value μ. According to the method of superposition, we set $f_1(\mu) = \frac{1}{2}$, $f_2(\mu) = (3/2)\,\mu^2$ and $c_1 = \frac{3}{4}$, $c_2 = \frac{1}{4}$. Thus, we obtain the expression

$$\mu = \begin{cases} 2\xi_2 - 1 & \text{if } \xi_1 < 3/4 \\ \left(2\xi_2 - 1\right)^{\frac{1}{3}} & \text{if } \xi_1 \geq 3/4 \end{cases}.$$

For higher photon energies, Eq. 18 is no longer valid and the distribution for the scattering angle α has to be derived from the differential Klein-Nishina cross-section (Eq. 7). As a more efficient method is not available, a rejection method is applied in this simulation (Wilms, 1996).

3.3 Simulation of interaction

In this Section, the formulas are presented which are used to simulate the scattering events. First, the scattering in Cartesian coordiantes is explained. To model scattering by hot electrons, a random velocity has to be drawn according to the relativistic Maxwell distribution. The derivation of the following equations in Section 3.3.1 and 3.3.2 are taken from Wilms (1996) and are listed here again anly for the sake of completeness.
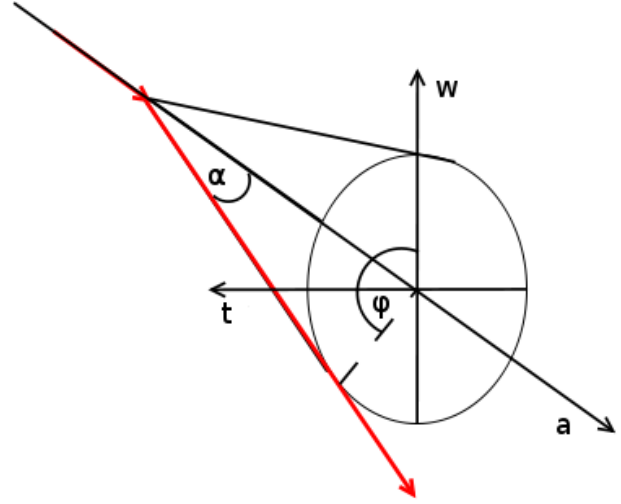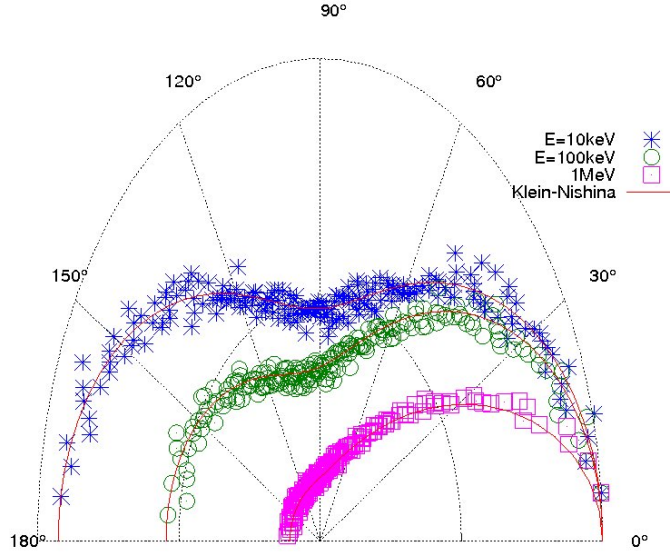
Figure 21: The sampled scattering angle α. For comparison, the differential Klein-Nishina cross-section is also plotted.

3.3.1 Scattering in Cartesian coordinates

If a photon is scattered by an electron, it will change its direction and energy. The change of direction is completely described by the azimuth direction angle φ and by the scattering angle α (see Fig. 20). The angle φ is uniformly distributed and can be modeled by using algorithm 1 (p. 34) in two dimensions. The scattering angle α is obtained from Eq. 7 with a rejection method (see Fig. 21).

To derive the new direction of the scattered photon, we assume that it was moving in a direction $\mathbf{a} = (a, b, c)$ with $|\mathbf{a}| = 1$ before the collision (c.f. Fig. 20). As the vectors $\{\mathbf{a}, \mathbf{w}, \mathbf{t}\}$ form a right-handed orthonormal basis, $\mathbf{w}$ is given by

$$\mathbf{w} = \frac{1}{\sqrt{a^2 + b^2}} \begin{pmatrix} b \\ -a \\ 0 \end{pmatrix}.$$

The third basis vector can be calculated from

$$\mathbf{t} = \mathbf{a} \times \mathbf{w} = \begin{pmatrix} a \\ b \\ c \end{pmatrix} \times \frac{1}{\sqrt{a^2 + b^2}} \begin{pmatrix} b \\ -a \\ 0 \end{pmatrix} = \frac{1}{\sqrt{a^2 + b^2}} \begin{pmatrix} ac \\ bc \\ -\left(a^2 + b^2\right) \end{pmatrix}.$$

The new direction of the photon in this coordinate system is

$$\mathbf{a}' = \begin{pmatrix} a' \\ b' \\ c' \end{pmatrix} = \begin{pmatrix} \cos\varphi \sin\alpha \\ \sin\varphi \sin\alpha \\ \cos\alpha \end{pmatrix} \tag{19}$$

With $\cos\alpha = \mu$, $\sin\alpha = \sqrt{1-\mu^2}$ and considering the definitions of $\mathbf{a}, \mathbf{w}, \mathbf{t}$, the new direction is calculated to

$$\mathbf{a}' = \mu \begin{pmatrix} a \\ b \\ c \end{pmatrix} + \sqrt{\frac{1-\mu^2}{a^2+b^2}} \left[\cos\varphi \begin{pmatrix} b \\ -a \\ 0 \end{pmatrix} + \sin\varphi \begin{pmatrix} ac \\ bc \\ -(a^2+b^2) \end{pmatrix} \right]$$

which can be also written as

$$a' = a\mu + (b\cos\varphi + ac\sin\varphi)\sqrt{\frac{1-\mu^2}{a^2+b^2}}$$

$$b' = b\mu + (-a\cos\varphi + bc\sin\varphi)\sqrt{\frac{1-\mu^2}{a^2+b^2}}$$

$$c' = c\mu - \sqrt{a^2+b^2}\sqrt{1-\mu^2}\sin\varphi.$$

As the term $\sqrt{1-\mu^2}$ is very susceptible for rounding errors if $\mu \approx 1$, it is replaced in the program by the expression $\sqrt{1-\mu^2} = \sqrt{(1+\mu^2)(1-\mu^2)}$. In case $a^2+b^2 \approx 0$, meaning the photon is moving almost into Z-direction or rather $\mathbf{a} \parallel \hat{z}$, the new direction is simply given by Eq. 19.

3.3.2   Generating hot electrons

To model radiative transfer through matter with a temperature $T \neq 0$, a Maxwell distributed random velocity for the target electron must be drawn every time a scattering event is simulated. Since the plasma around X-ray sources can reach very high temperatures, the relativistic Maxwell distribution is needed. The original algorithm was implemented by Wilms (1996) written in FORTRAN and the following derivation is taken from there. A C-version of this algorithm was written and added to the simulation by Nekovar (2012).

In the following, the convention $m_e = c = k = 1$ is used. The distribution function of free particles with energy $\varepsilon(p, q)$ is given by:

$$n(p) \propto \frac{N}{V} \exp\left(-\varepsilon(p)/T\right). \tag{20}$$

In the relativistic regime is $\varepsilon^2 = 1 + p^2$, we get from Eq. 20

$$n(p)\mathrm{d}^3p = 4\pi \frac{N}{V} \exp\left(-\beta\sqrt{1+p^2}\right) p^2 \mathrm{d}p$$

with $\beta = T^{-1}$. To normalize the distribution, it is integrated over the entire momentum space

$$\int_0^\infty \exp\left(-\beta\sqrt{1+p^2}\right) p^2 \mathrm{d}p = \int_0^\infty \exp\left(-\beta\cosh(t)\right) \sinh^2(t)\cosh(t)\,\mathrm{d}t.$$

The McDonald function is defined by

$$\frac{K_1(z)}{z} = \int_0^\infty \exp\left(-z\cosh(t)\right) \sinh^2(t)\mathrm{d}t$$

$$\frac{d}{dz}\left(\frac{K_1(z)}{z}\right) = \int_0^\infty \exp\left(-z\cosh(t)\right)\sinh^2(t)\cosh(t)\,dt.$$

With the relations

$$\frac{dK_1(z)}{dz} = -\frac{K_1(z)}{z} - K_0(z)$$

$$\frac{d}{dz}\left(\frac{K_1(z)}{z}\right) = -\frac{2K_1(z)}{z^2} - \frac{K_0(z)}{z}$$

the relativistic Maxwell distribution is given by:

$$n(p) = 4\pi \frac{N}{V} \frac{\exp\left(-\frac{1}{T}\sqrt{1+p^2}\right)p^2\,dp}{2T^2 K_1\frac{1}{T} + TK_0\frac{1}{T}}. \tag{21}$$

.

3.4 Geometry

The shape of the resulting spectrum depends much on the geometry of the absorbing material. The extension of the cloud and its position relative to the source decides how many particles are located actually along the line of sight. In this thesis, two different geometries are used: the spherical geometry where the source is embedded in a cloud and the slab geometry in which the source may be located above or onto a infinitely extended plain. In the last case, only the reflected radiation is of interest.

For each geometry, algorithms are needed that propagate the photon through the medium and determine whether it is escaped. Since this routines are called many times during a simulation, the methods should be programmed very efficiently. The current position of a photon is denoted by $\mathbf{x}_0 = (x_0, y_0, z_0)$ and its direction by $\mathbf{a} = (a, b, c) = (\cos\varphi\sin\vartheta, \sin\varphi\sin\vartheta, \cos\vartheta)$ with $|\mathbf{a}| = 1$. The path of the photon is than given by

$$\mathbf{x} = \mathbf{x}_0 + t\mathbf{a} \tag{22}$$

with $t > 0$.

For simplicity, the units of this lengths are calculated in Thomson optical depths τ_T. For a medium with the extension R, the relation between R and the cloud's τ_T is given by

$$\tau_T = \sigma_T n_e R \tag{23}$$

where σ_T is the Thomson cross-section and n_e the electron number density. By setting $n_e = 1/\sigma_T$, one optical depth is equal to one unit of lenght. The density of the medium can than be varied by changing R. The hydrogen column density is obtained by

$$N_H = \frac{n_e}{\left(\frac{n_e}{n_H}\right)} R$$

with the hydrogen density n_H. The ratio n_e/n_H gives the number of electrons per hydrogen atom and depends on the elemental mixture of the cloud.

3.4.1 Spherical cloud

The geometry of a spherical cloud is used to obtain transmitted spectra. As a sphere is symmetric in each direction, all out-coming photons can be considered as equivalent regardless of where or under which angle they were escaping. To draw a random pathlength (compare with 15, step 2) for a photon located at position $\mathbf{x}_0$ and traveling in direction $\mathbf{a}$, the distance L to the medium's edge has to be known.
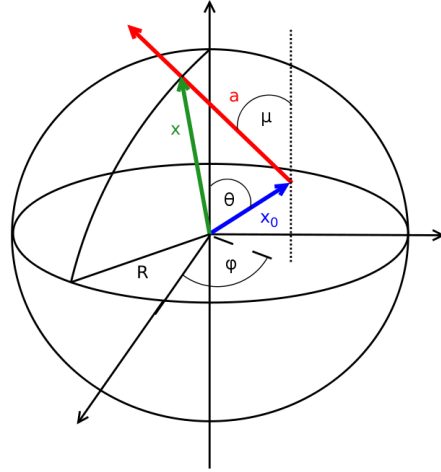
In Figure 22, a skatch of this situation is shown. We have to compute the point x where the photon leaves the sphere. Thus, the distance can be calculated to $L = |\mathbf{x} - \mathbf{x}_0|$. Considering that the intersection point will lie on the surface of the sphere which means $|\mathbf{x}| = R$ and with Eq. 22, we get

Figure 22: Skatch to the path computation in a sphere geometry.

$$R^2 = \mathbf{x}^2 = (\mathbf{x}_0 + t\mathbf{a})^2 = (x_0 + ta)^2 + (y_0 + tb)^2 + (z_0 + tc)^2$$

which can be written as

$$At^2 + 2Bt + C = 0 \tag{24}$$

with

$$A = a^2 + b^2 + c^2 = 1$$
$$B = ax_0 + by_0 + cz_0$$
$$C = x_0^2 + y_0^2 + z_0^2 - R^2.$$

The solution of Eq. 24 is than given by

$$t_{1,2} = -B \pm \sqrt{B^2 - C}$$

and we will assume $t_1 > t_2$. For a more general deviation in the case the photon source is located outside the sphere, see the manual belonging to the simulation from Wilms (1996).

In Figure 23, a three dimensional plot of one hundred photon pathes simulated for a spherical cloud with radius $\tau = 10$ is shown.

A source located in the center of the cloud emits isotropically monochromatic photons with $E = 100$ keV. As the cloud is very opaque with a Thomson optical depth of 10, only few photons, that are down-scattered to low energies can escape.

3.4.2 Slab

The reflected spectra presented in this thesis are simulated in a semi-infinite slab geometry. A photon source is located above an infinitely extended plane which has an optical depth of ∞ . By irradiating slabs, the spectra of radiation that is reflected, for example, by accretion disks can be
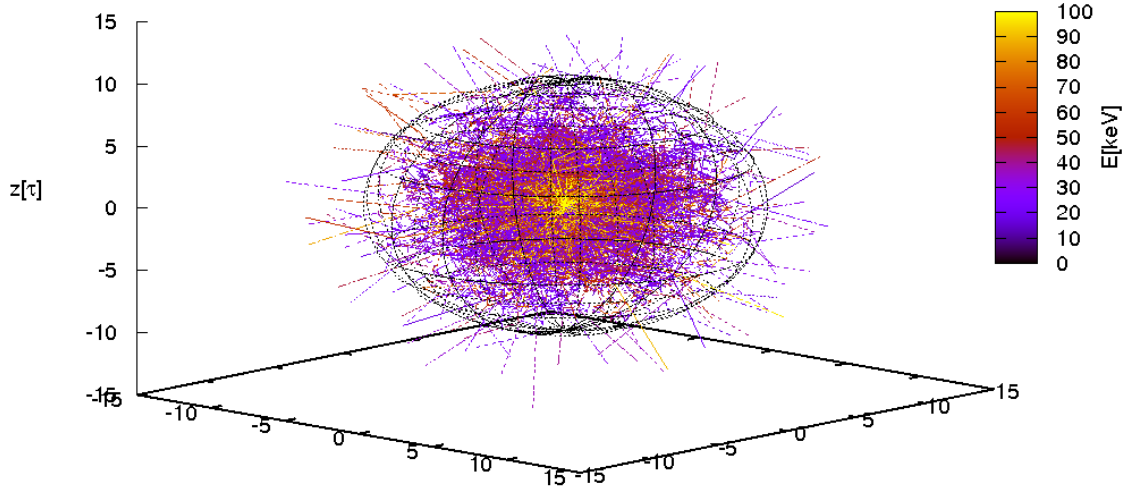
Figure 23: Hundred photon paths simulated in a spherical cloud with radius $\tau = 10$

modeled. In this geometry, the angle between the normal of the slab and the direction of the out-coming photons is of interest. Since only the distance to the surface in photon's moving direction decides about the current optical depth, the photon has to be propagated just in two dimensions. Assuming the slab is extended in the x-y plane and infinite in -z direction. A photon is located at position $\mathbf{x}_0$ and has a direction $\mathbf{a}$. We test first whether the photon is moving upwards in direction of the edge or downwards. If it is traveling downwards, we just draw a τ and propagate the photon. In the other case, the distance to the medium's edge is given by $L = |z_0/c|$.

In Figure 24, thousand photon pathes are plotted.

The source is located at $\tau = 20$ above the plane and marked by a blue circle. The emitted photons have all an energy of 100keV and a direction $\vec{a} = (0, 0, -1)$. How one can see, the primary beam can be followed up to an optical depth of ~ -5 until it is completely split up. The escaping photons seemed to be reflected just beneath the surface during the mainly part that gets deeper in the medium is scattered around until it can be absorbed. To avoid senseless computation time all photons with z-coordinate < -5 are considered as absorbed.
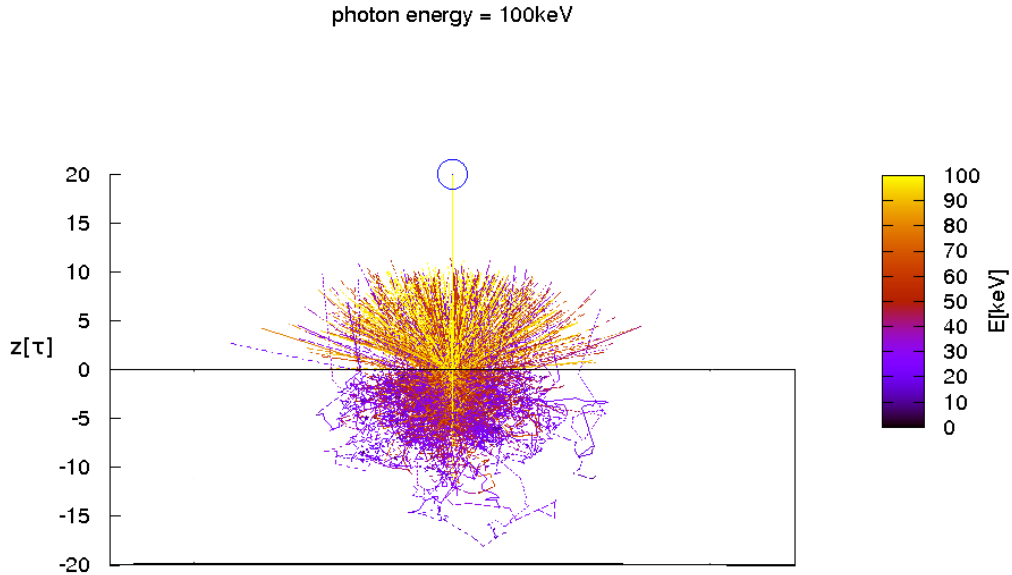
Figure 24: Illustration of a semi-infinite slab geometry with a photon source located at $\tau = 20$ above the plane.

4   X-ray absorption in cold matter

The presence of a large amount of cold matter is well established around Active Galactic Nuclei (Matt et al., 1999). In the spiral galaxy NGC 4945 for example, the column density is about $\sim 10^{24.7}$ cm^{-2} (Iwasawa et al., 1993) and the flat spectra of Seyfert II galaxies indicate column densities exceeding 10^{25} cm^{-2} (Maiolino et al., 1998). X-ray absorption by cold matter in meaning of not much ionized and substantially opaque is a common phenomenon also in X-ray binary systems, especially in wind-fed systems (see Section 2.1.3) with column densities in the range $\sim 10^{23} - 10^{24}$ cm^{-2} (White et al. (1995), p. 43).

The eclipsing high mass X-ray binary Vela X-1 is an example of such a system. Vela X-1 consists of a neutron star and a super-giant B-type star with an orbital period of 8.964 days. The companion star has a mass of ~ 25 M$_\odot$ and a radius of ~ 30 R$_\odot$ (see Kreykenbohm (2004) and references therein) . The neutron star is deep embedded in the super-giants stellar wind resulting in strongly absorption of the X-ray spectra. The degree of absorption is thereby dependent on the orbital phase and increases at the eclipse when the neutron star is moving through the dense inner region of the stellar wind (Haberl & White, 1990). In Figure 25, the pulsed averaged spectra calculated by Sato et al. (1986) for different phases around the eclipse are shown.

At phase $\Phi = 0.0$ the eclipse takes place and from I to VI, the neutron star is emerging from the innermost regions into less dense stellar wind. The spectrum I at $\Phi = 0.049 - 0.099$ has a strong iron K absorption edge and emission line around $6 - 7$ keV which is typical for highly absorbed
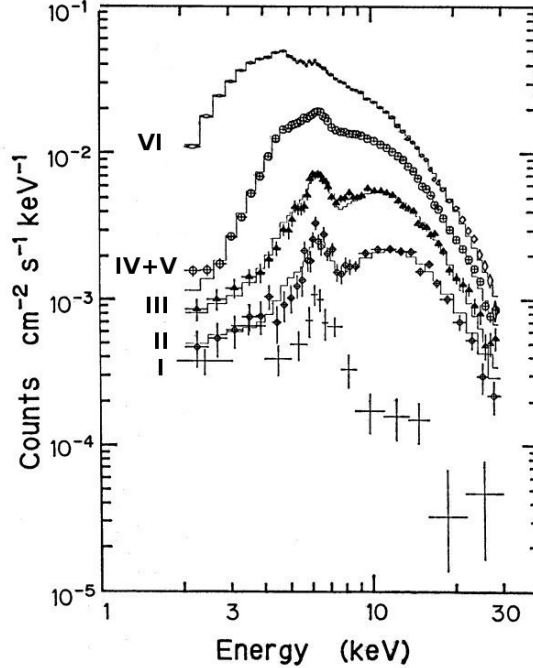
Figure 25: The pulse averaged spectra of Vela X-1 observed throughout the eclipse: $\Phi = 0.049 -$ 0.099 (I), $\Phi = 0.106$ (II), $\Phi = 0.114$ (III), $\Phi = 0.121$ (IV), $\Phi = 0.127$ (V), $\Phi = 0.179$ (VI) (from Sato et al. (1986)).

spectra while spectrum V observed at $\Phi = 0.179$ is already almost featureless.

The shape of the measured spectrum depends strongly on the geometry of the absorbing material. When the matter is located along the line of sight, we substantially observe a transmitted spectrum but often with a reflected component that may indicate the presence of an accretion disk.

In this section, I will present the transmitted and reflected spectra as obtained from the Monte Carlo simulation. The transmitted spectra were produced using a spherical geometry and are calculated for different column densities. In the reflected case, a point source is located upon a semi-infinite slab and emitts photons isotropcally. Thus, the observed spectra are angle-dependent. The spectra for both geometries were compared to established models within the X-ray data analysis package XSPEC (Arnaud, 1996).

4.1 Transmitted spectra

The shape of the spectra described above can be understood by considering the different involved interaction mechanisms between radiation and matter. Photoabsorption is the dominating process for a photon energy below $\sim 10\,\mathrm{keV}$ and therefore a large fraction of the photons is absorbed in this range. The absorptivity is $\propto E^{-3}$ for X-rays (see Eq. 9) and for photon energy above 10 keV , the opacity is mainly determined by Compton scattering with electrons (Figure 10).

If the medium is dense enough to allow frequently interactions, scattering will influence also

the shape of the spectrum, particularly in the high energy range. Equation 4 can be written as

$$\frac{\Delta E}{E} = 1 - \frac{1}{1 + \frac{E}{mc^2}(1 - \cos \alpha)} \tag{25}$$

where $\Delta E = E - E'$ is the difference between the energy E of the incident photon and the scattered one. Considering Eq. 25, the relative energy loss $\Delta E/E$ after one scattering increases with increasing energy E and therefore a high energetic photon will suffer a larger energy loss than a low energetic one. If the former collides with a an electron, it is easily down-scattered to energies where absorption becomes possible.

For these reasons we expect a spectrum with little photons on the low energy end and a significant modification of the input spectrum in the high energy range due to Compton scattering only for highly obscured sources. In addition, the fluorescence lines should become more intensive for higher degrees of absorption, since more line photons can be emitted along the line of sight.

4.1.1 General shape

In Figure 26, the transmitted spectra for different column densities are plotted together with the incident spectrum. Only K_α-lines are emitted in this example (compare with method of weights on page 29), other line emission is suppressed.
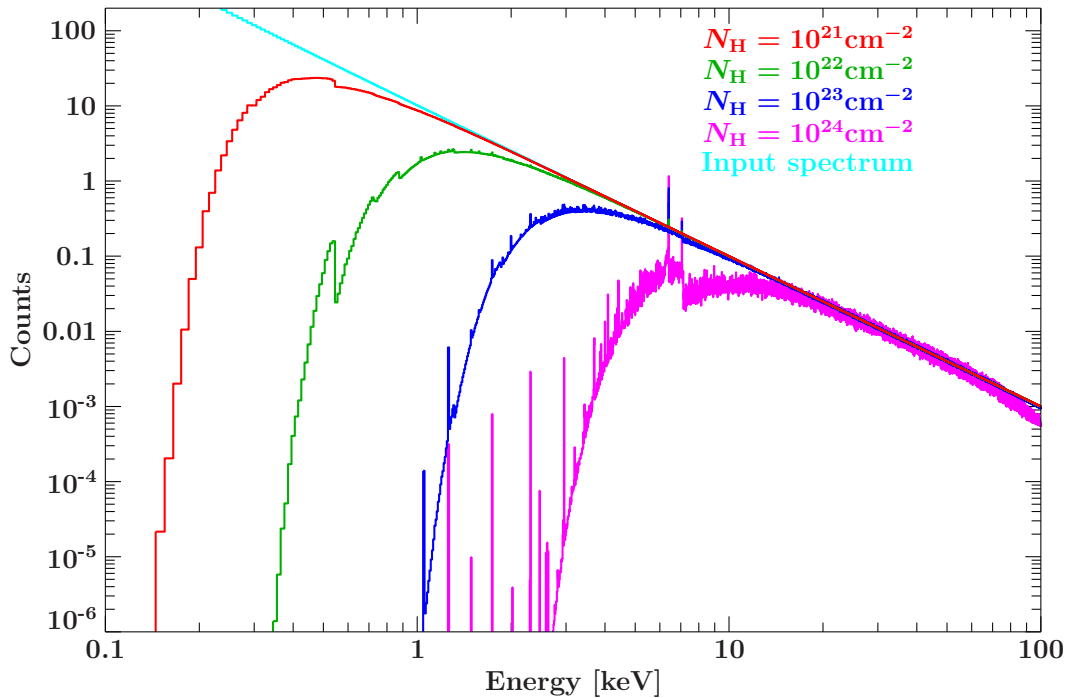

Figure 26: Transmitted spectra for various column densities.

The spectra are simulated for an incident powerlaw with photoindex $\Gamma = 2.0$ using the spherical geometry explained in Section 3.4.1. The photo-ionization cross-sections are those from Verner & Yakovlev (1995) and the elemental abundances from Wilms et al. (2000) are adopted. The electron temperature is set to 0 K.

The red curve ($N_H = 10^{21}$ cm^{-2}) shows a transmitted spectrum when only a small amount of matter is located in line of sight. Due to the low density the majority of photons escapes unhindered

and only for energies below ∼ 1 keV the spectrum is significantly absorbed. In this case no emission lines are seen since the few line photons are completely covered by the photons escaping without a check (primary emission). At ∼ 0.5 keV the O K-absorption edge ($E = 0.533$ keV) becomes visible. For energies above ∼ 2 keV there is no absorption recognizable and the shape of the spectrum is determined by the incident spectrum. This is because Compton scattering is not important for such low densities and only few photons are scattered overall.

The next higher absorbed spectrum (green curve) is simulated for $N_H = 10^{22}$ cm^{-2}. Here significantly more photons are already absorbed up to ∼ 2.5 keV. The O K-edge is now very pronounced and more absorption edges emerge from the primary emission like the Ne K-edge at 0.876 keV and the Mg K-edge at 1.309 keV. The fluorescence lines are still mainly overlapped by the continuum, but single weak lines like the Na K$_\alpha$ -line ($E = 1.041$ keV) and also the Fe K$_\alpha$ -line ($E = 6.404$ keV) are visible. For energies above ∼ 3 keV the shape of spectrum is basically given by the input spectrum due to scattering events are still rare.

This changes for the blue spectrum simulated with a column density $N_H = 10^{23}$ cm^{-2}. No photon with an energy below ∼ 1 keV is able to escape from the medium and the spectrum shows absorption features up to 10 keV. The Fe K-edge is observable at $E = 7.112$ keV together with some strong fluorescence lines particularly Na, Mg and Fe. Around ∼ 10 keV more and more high energetic photons are down scattered and the transmitted spectrum starts to slip below the incident one. It is now likely that a high energetic photon is scattered at least once before escaping the medium and multiple scatterings becomes more important. For this reason, the contours of the spectrum appears more smeared out than the ones described before.
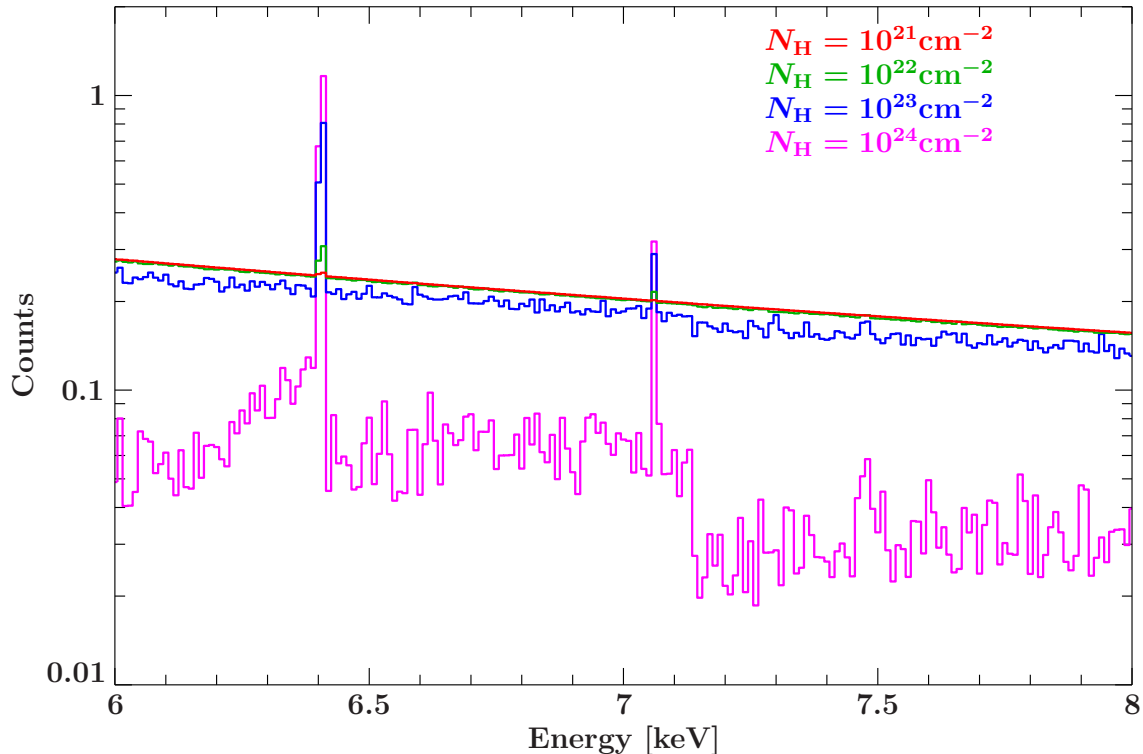

Figure 27: Same as Figure 26 with more detailed view on the iron band.

This effect is evident by viewing at the last spectrum (magenta curve, simulated for $N_H = 10^{24}$ cm^{-2}). Additionally, the simulated spectrum lies clearly below the input spectrum above

~ 70 keV due to effective down scattering from high energetic photons. In the lower energy range between ~ 1 keV and ~ 3 keV only line photons are visible because the primary emission is almost completely absorbed in this energy range. s

The strong iron line shows a clearly visible Compton shoulder as shown in detail in Figure 27. The Compton shoulder is a feature formed by line photons, that are scattered at least once before escaping. The Compton shoulder exists also for column densities below ~ 10^{24} cm^{-2} (compare with Fig. 39), but it is completely covered by the primary emission. Only when the medium is so dense that a significant fraction of the input photons are absorbed in the energy range around the iron line, the Compton shoulder becomes visible.

4.1.2 Comparison with the absorption model `tbabs`

To comparison and code verification, the simulated data was compared to the absorption model `tbabs` implemented by Wilms et al. (2000). The fits in Figure 28 were performed by fixing the powerlaw index to the value for which the data was simulated ($\Gamma = 2.0$) leaving the column density N_H as free fit parameter. Since in the model `tbabs` no fluorescence lines are taken into account, the line emission was suppressed in this simulations for better comparison. The best fits are shown for N_H between 10^{21} cm^{-2} and 5×10^{24} cm^{-2} . Additional to the spectra, the variation rate from the model is also plotted. The green label is the value of N_H used in the simulation while the red one denotes the best fit value. The deviations above ~ 1 keV as well as those around the pronounced iron K-edge are discussed in more detail below. The model adaption around the absorption edges is more successful when a smaller grid is used. But the use of a smaller grid leads to a high noise rate especially in the high energy range where the spectrum is modified significantly by Compton scattering. To represent this important range well, the model is rather fitted in a wider energy grid. To illustrate the differences between the Monte Carlo model and `tbabs`, the same spectra were fitted again by fixing N_H at the simulation parameter. The results are shown in Figure 29.

For column densities $\lesssim 10^{22}$ cm^{-2} the data agrees well with the model above ~ 1 keV as seen on the first two plots in Figure 28 but the best-fit value of N_H underestimates the actual simulation parameter for $N_H \lesssim 10^{22}$ cm^{-2} and this effect is more significant for lower column densities. For $N_H = 10^{21}$ cm^{-2}, the calculated value deviates from the parameter set by almost ~ 20% since between $N_H = 10^{22} - 10^{23}$ cm^{-2} the deviation is only $1 - 4\%$. The spectrum for $N_H = 10^{23}$ cm^{-2} shows an additional deviation from the model for high energies: the count rate is significantly below the model for energies $\gtrsim 80$ keV. The reason for this is the influence of Compton scattering as explained in the section before: high energetic photons loose a bigger fraction of its energy via collisions with electrons then low energetic ones and are scattered down to lower energies. This effect is more evident for the higher absorbed spectra as seen in the plots for $N_H = 5 \times 10^{23} - 5 \times 10^{24}$ cm^{-2}. Particularly the spectrum simulated for $N_H = 5 \times 10^{24}$ cm^{-2} shows an obvious lack of photons above ~ 50 keV and a bump formed by the down-scattered photons at ~ $15 - 50$ keV. Due to the lower count rate in the high energy range, the column density is overestimated for a simulation parameter $N_H > 10^{23}$ cm^{-2}.

The differences between the simulated data and the model particularly in the high energy range exists because `tbabs` does not include the absorption by Compton scattering. Within the model, the absorption by gas-phase interstellar medium is calculated by summing over the photo-ionization cross-section of the different elements whereas Compton scattering is not considered.
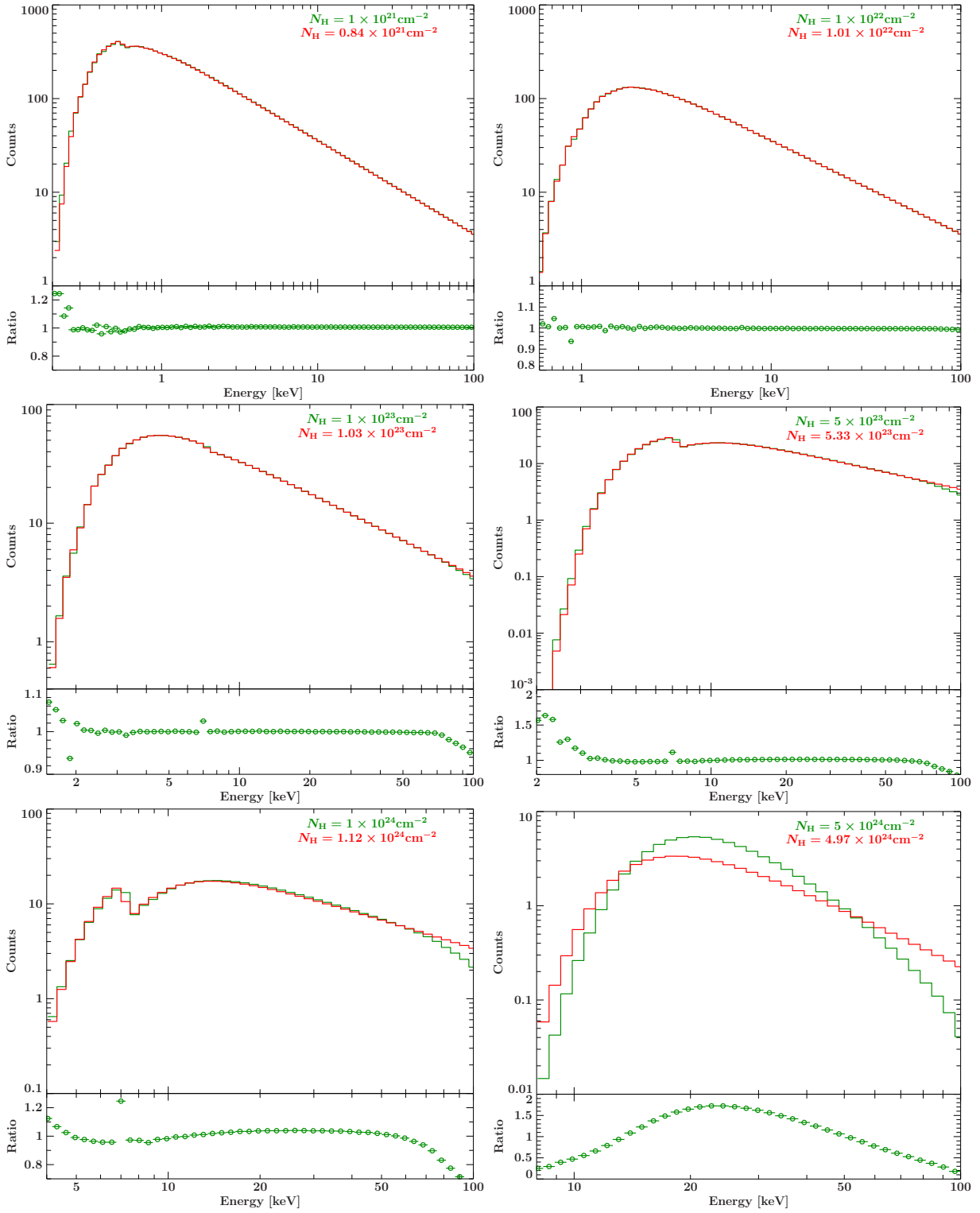
Figure 28: Comparison between the simulated spectra and the absorption model `tbabs` for column densities $1 \times 10^{21} - 5 \times 10^{24}$ cm^{-2}. The green label denotes the simulation parameter and the red one is the best-fit parameter. N_{H} is let as free parameter.
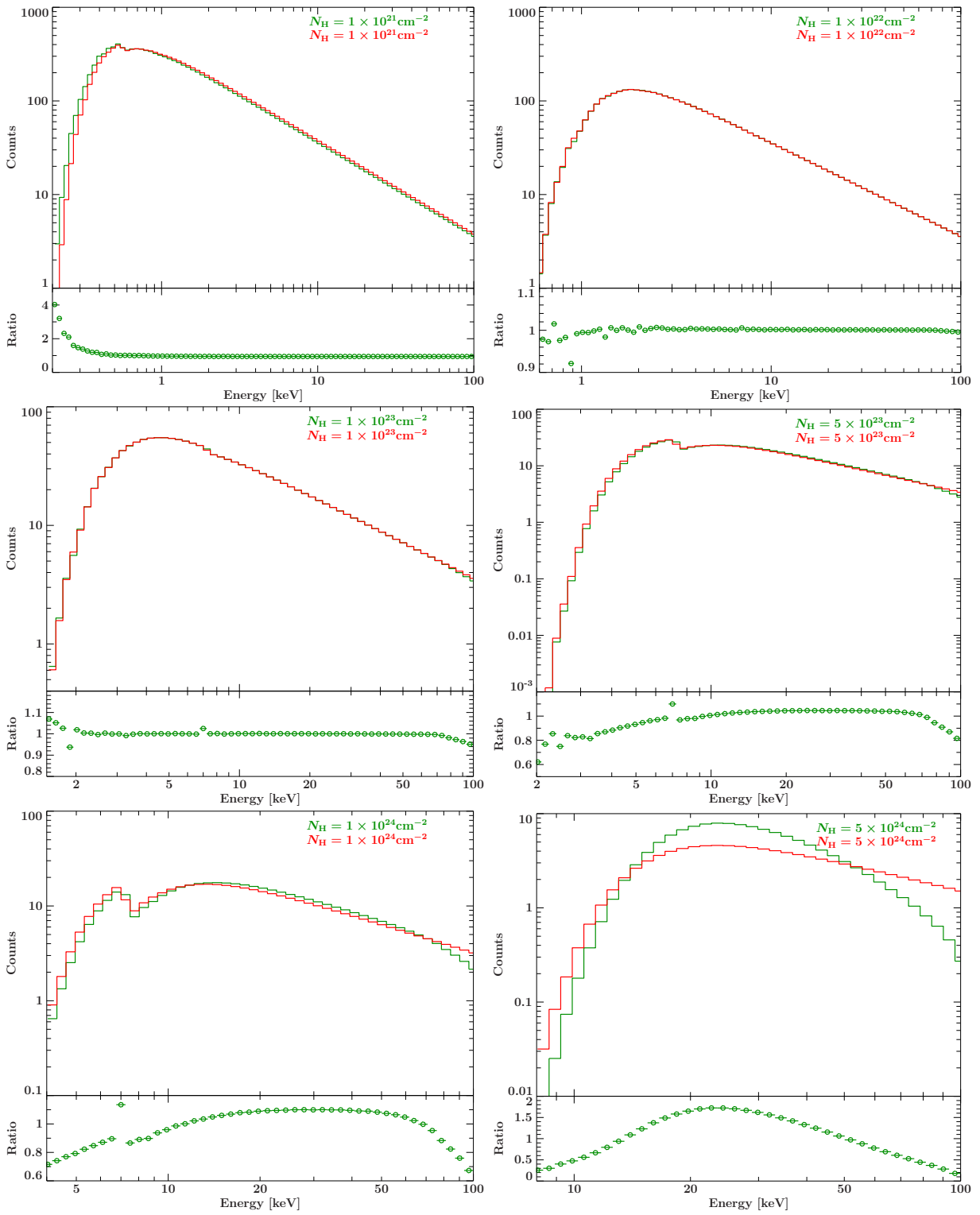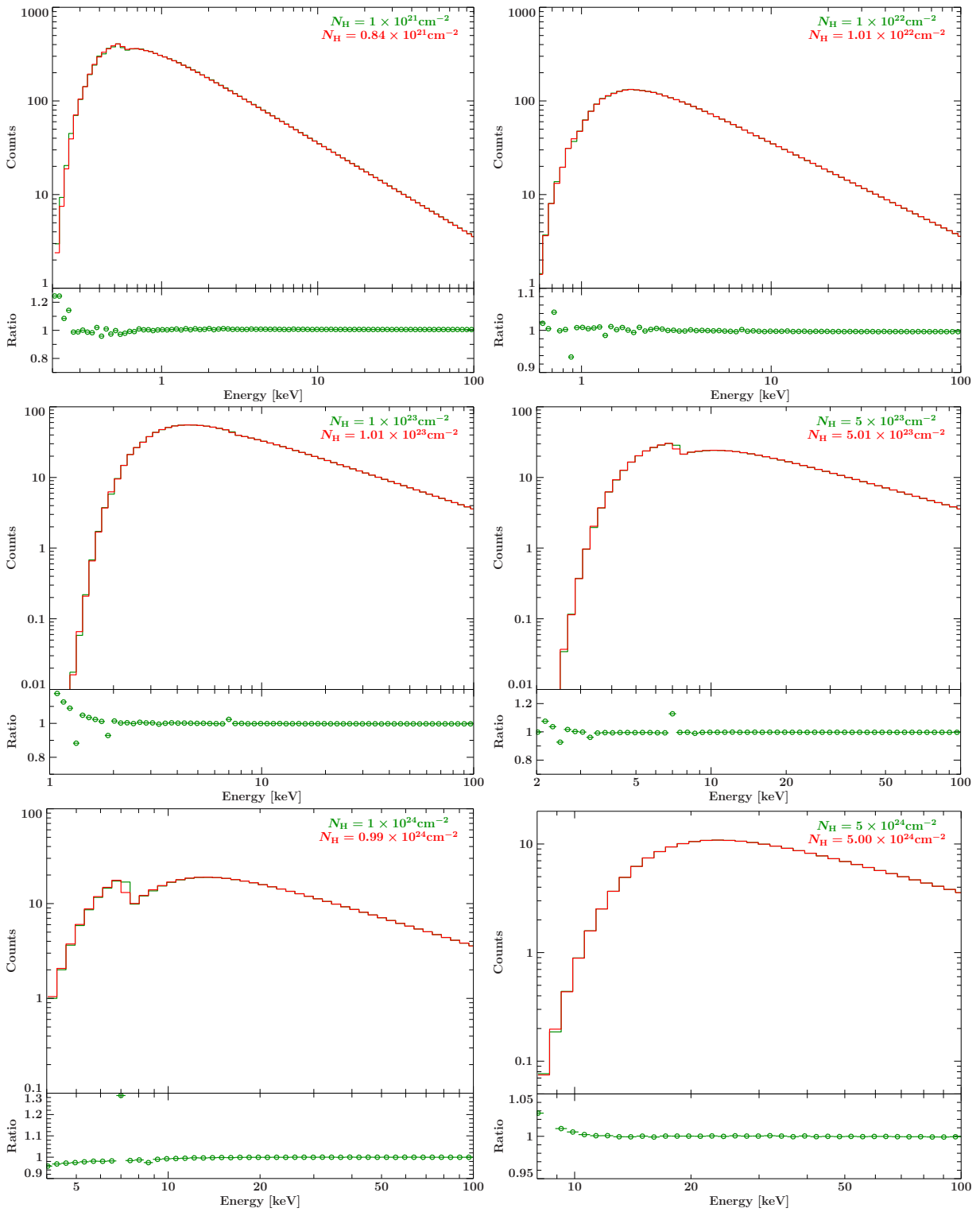
Figure 29: Same as Figure 28, but with fixed N_H.

Figure 30: Same as Figure 28 but the spectra are simulated by considering photo-absorption alone

At energy E and for a hydrogen number density N_H along line of sight, the intensity is computed as

$$I_{\text{out}}(E) = \exp\left\{-\sigma_{\text{ISM}}(E)N_H\right\} I_{\text{in}}(E)$$

where σ_{ISM} is the photoabsorption cross-section and I_{in} the intensity of the incident spectrum (see Wilms et al., 2000). If Compton scattering is also taken into account, the transmitted spectrum is instead obtained by calculating

$$I_{\text{out}}(E) = \exp\left\{-\sigma_{\text{ISM}}(E)N_H - \sigma_C(E)N_E\right\} I_{\text{in}}(E)$$

with the Klein-Nishina cross-section σ_C and the electron number density N_E.

To make sure that the neglegect of scattering actually leads to the deviations in the high energy range, several spectra were simulated by considering Compton-scattering alone and were fitted again with `tbabs`. The results are shown in Figure 30. It is not hard to see that the model fits the data perfectly in the high energy range.

To estimate the error that is made when N_H is calculated without considering Compton scattering, several spectra for different column densities between 10^{22} cm^{-2} $- 9 \times 10^{24}$ cm^{-2} were produced and fitted by leaving N_H as free fit parameter. In figure 31 the deviations between the values $N_{H,\text{Model}}$ calculated as best fit parameters by `tbabs` and that ones actually used as simulation parameters $N_{H,\text{Sim}}$ are plotted as a function of $N_{H,\text{Sim}}$. As one can see, neglecting Compton scattering leads to an overestimation of the column density for $N_{H,\text{sim}}$ between 10^{23} cm^{-2} and a few times of 10^{24} cm^{-2}. The fitted values exceed clearly ($> 10\%$) those for which the spectra were simulated at $N_H \approx 10^{24}$ cm^{-2}. Approximately in this range, multiple scatterings becomes important. For column densities $\gtrsim 2 \times 10^{24}$ cm^{-2} the deviator seems to become smaller, but as the plot for $N_H = 5 \times 10^{24}$ cm^{-2} in Figure 28 shows, the model can not fit the data for these degrees of absorption.
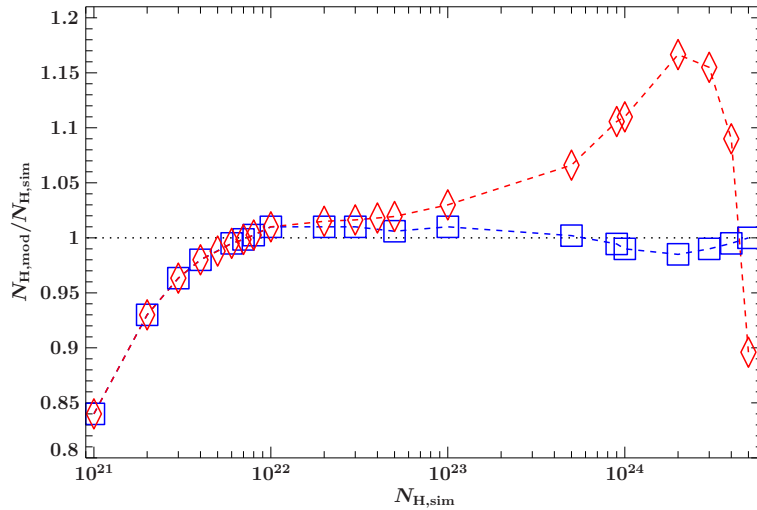

Figure 31: Comparison between simulation and the absorption model `tabs`. The green symbols refer to the case when Compton scattering and photo-absorption is taken into account and the blue ones are for photo-absorption alone.

The reason for this overstimation becomes clear by comparing the fits for $N_H = 1 \times 10^{24}$ cm^{-2} in Figure 28 and Figure 29. If N_H is fixed on the simulation parameter, one can see that the count rate lies below the model for photon energies $< 10\,\text{keV}$. This comes from the additional absorption
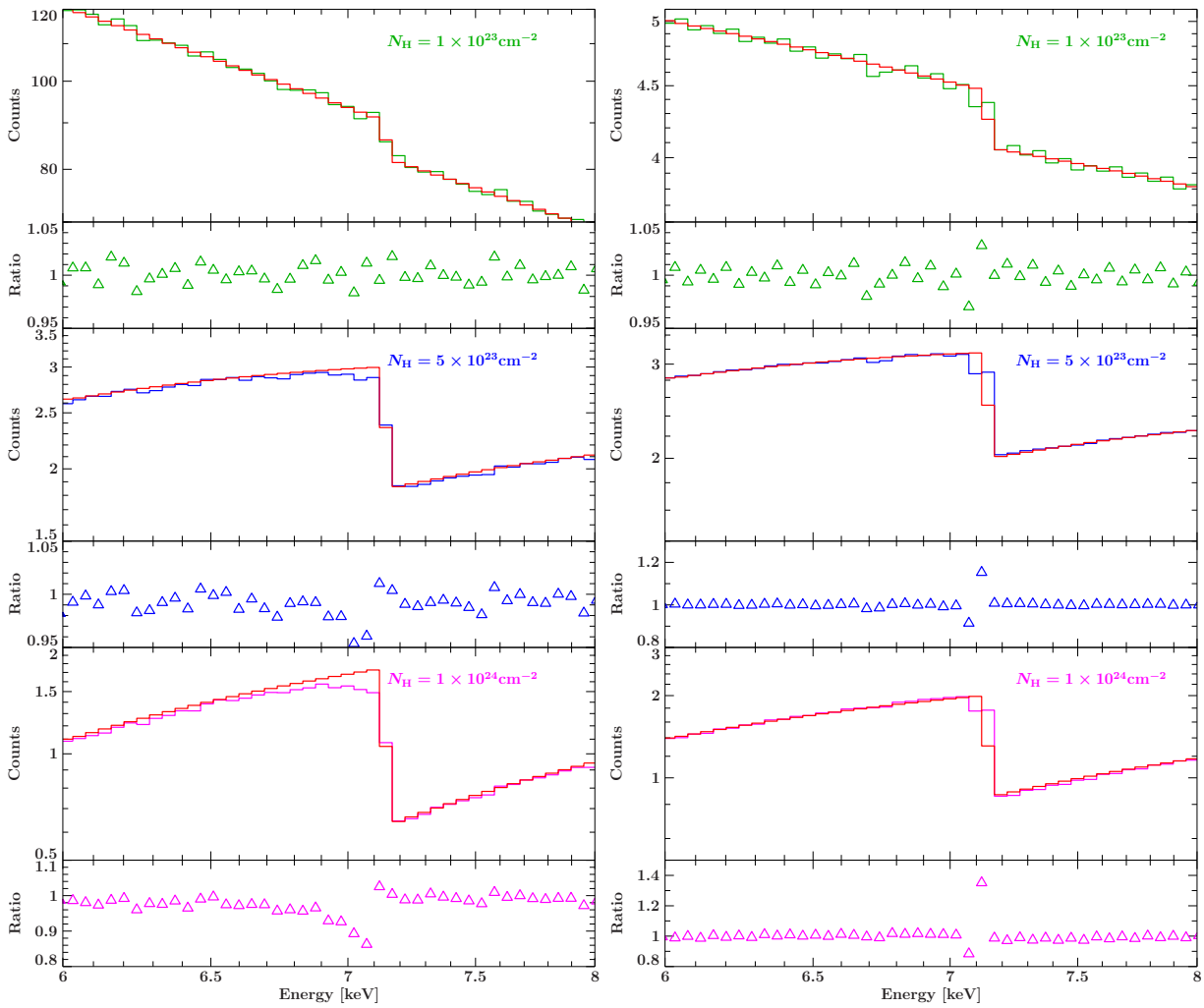
Figure 32: Comparison with `tbabs` with detailed view on the iron K-edge. On the left side, the spectra were simulated by including Compton scattering and those ones one the right side by ignoring it.

due to Compton scattering. Is on contrast N_{H} left as free fit parameter, the model adaption in this energy range leads to the calculation of a higher degree of absorption as is indeed the case.

As mentioned before and seen in the fits for column densities of $1 \times 10^{23} \text{cm}^{-2}$, $5 \times 10^{23} \text{cm}^{-2}$, and $1 \times 10^{24} \text{cm}^{-2}$ (see Figure 28), the model does not agree well with the data around the iron K-edge. This feature is also seen in the spectra which were produced by considering photo-absorption alone (Fig. 30). Therefore, the deviation is not from Compton scattering alone. To consider this deviation in more detail, the model `tbabs` is evaluated on a smaller energy grid and the results are shown in detail in Figure 32 for this energy range. The spectra on the left side were produced by considering Compton scattering and those on the right by ignoring this process. The simulation´s parameters are the same as for the spectra in Figure 28. Compton scattering has an influence on the shape of the absorption edge as seen in the plots on the left side. The top spectrum simulated for $N_H = 1 \times 10^{23} \text{cm}^{-2}$ agrees still quiet well with the model. This is not the case for greater column densities. Particularly the left side of the iron K-edge is reduced with respect to the model as seen in the spectrum for $N_H = 5 \times 10^{23} \text{cm}^{-2}$. This effect becomes more significant in the last spectrum for $N_H = 1 \times 10^{24} \text{cm}^{-2}$. As seen in the plots on the right side, the data agrees almost perfectly with the model below and above the absorption edge. The data deviates only exactly at the sharp edge. Since the spectral shape changes abruptly at the iron K-edge energy, the binning in this energy raneg is difficult and may lead to this unwanted feature. Therefore, the peak-like deviation around the absorption edge as seen in Figure 28 has mostly no physical meaning.

As denoted earlier, `tbabs` underestimates the value of N_H slightly for column density $< 10^{23}$ cm^{-2}. This is also the case when Compton scattering is excluded as seen in Figure 31. Considering the plots in Figure 29, in particular the fit for $N_H = 1 \times 10^{21}$ keV, the data deviates from the model especially in the low energy range. One possible explanation for this deviation would be that either sligthly different photo-absorption cross-section are used.

4.2   Reflected spectra

In the transmitted case, the absorbing matter is located between source and observer in the line of sight. In contrast, Compton reflected spectra originates from radiation that is back scattered by material sourounding the compact object. In this picture, the X-ray source is located upon a slab, usually the accretion disk, and the reflected primary spectrum is modified by Compton-scattering and bound-free absorption (Magdziarz & Zdziarski, 1995). In such a system which could be a AGN or a X-ray binary, cold matter coexists very close to hot matter near the center of the compact object and the observed spectrum is a composition of the primary radiation emitted directly by the source and a reflected part of it.

In Figure 33, the typical spectral components of an unobscured AGN is shown as described by Fabian (2006). In addition to the underlying power-law and the soft excees that originates from thermal blackbody emission, a reflected component is fitted together with a strong iron line. The reflected part is limited in the lower energy range by photo-absorption and the upper limit is determined by electron scattering (Lightman & White, 1988). Since the relative energy loss in a scattering process is larger for high energy photons as still discussed in Section 4.1, a bump of down-scattered photons above ~ 10 keV appears.

If the slab is illuminated with photons between 100 keV and 1 MeV, about 10% of the radiation is reflected (Wilms, 1996), dependent on the viewing angle.

As Wilms (1996) described in his diploma thesis, the reprocessed spectrum f_{refl} is usually considered as an additional fit component to the primary emission f_{prim}. The entire observed spectrum
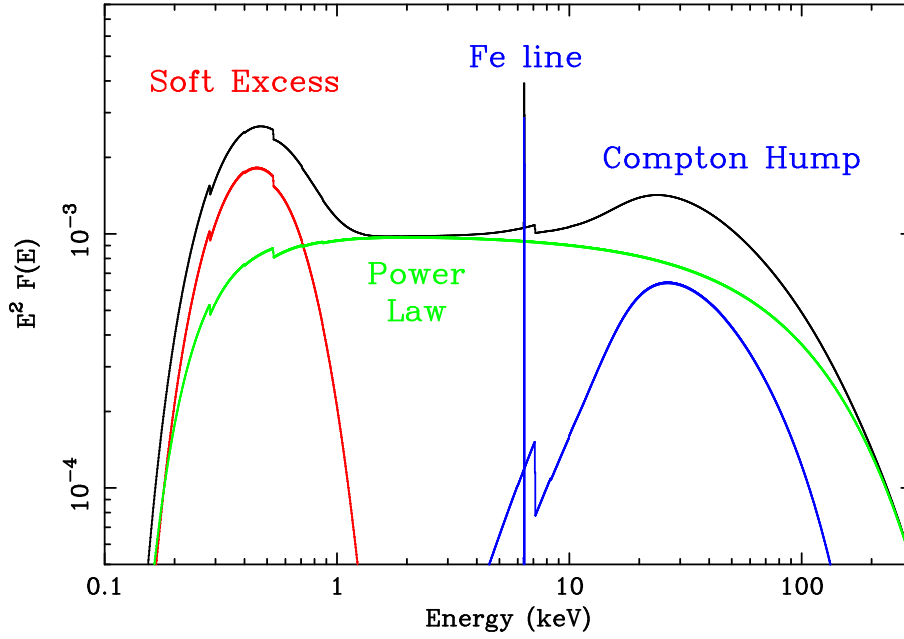
Figure 33: Modeled X-ray spectrum of an AGN (from Fabian, 2006). The hump at $10 - 100$ keV in the entire spectrum (black curve) comes from Compton reflection (blue curve).

is than given by

$$f_{obs} = f_{prim} + A f_{refl} \tag{26}$$

where A is called the *covering factor*. This factor describes the ratio between the reflected and the non-reflected emission. As Wilms (1996) remarks, A can be greater than one due to its stonf mathematical definition and has no geometrical meaning in Eq. 26. In addition, f_{refl} is not necessarily generated by f_{prim}. If we assume a slab with angular expansion Ω located below a point source emitting a spectrum $f_{inc}(E)$ isotropcally, the observed spectrum can be written as

$$f_{obs} = f_{inc}(E) + \frac{\Omega}{2\pi} f_{refl}(f_{inc}, E). \tag{27}$$

Only if $f_{prim} = f_{inc}$ and $A < 1$, a geometrical interpretation is justified.

4.2.1 Angle averaged spectrum

In Figure 34 the reflected spectrum averaged over all inclination angles is shown for different input photon-powerlaws. As described above, the reflection is assumed as an additional spectral component to the primary emission. Therefore, the sum of input and reprocessed spectrum is also plotted.
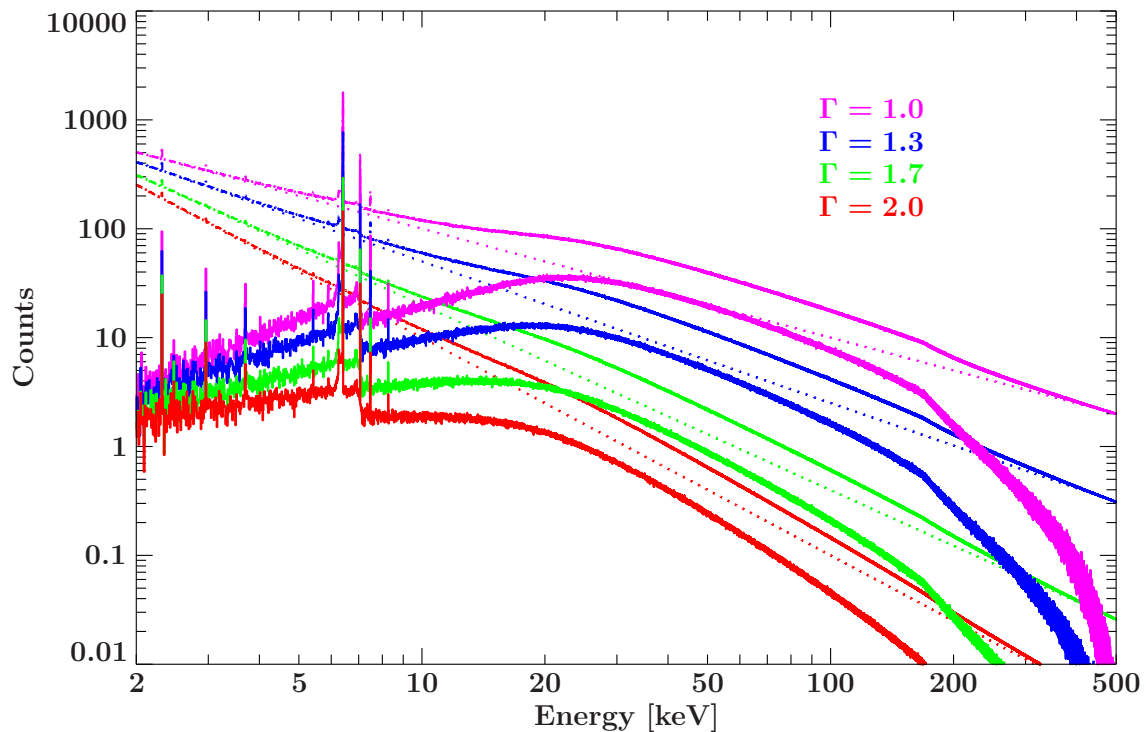
Figure 34: Reflected spectrum averaged over all inclination angles for different incident powerlaws with photoindex Γ. The input spectrum (dotted line) as well as the sum of primary emission and reflection are also plotted.

The hump at $10 - 100$ keV which is typically for Compton reflection is well seen, especially for small Γ. Considering Eq. 14, a smaller photoindex means that more photons are emitted at higher energies. Since the hump mainly consists of down-scattered high energy photons, it grows with decreasing Γ. Depending on which fractional part of the primary emission is reflected, the hump emerges significantly from the primary emission. The sharp kink around ~ 200 keV comes from the input powerlaw being brocken off at 500 keV and has no physical meaning. Since below ~ 10 keV the photo-absorption cross-section is high with respect to Compton scattering, only few continuum photons are reflected in this range. Therefore, the fluoresence lines are very strong in the reflected spectra, especially those from iron.

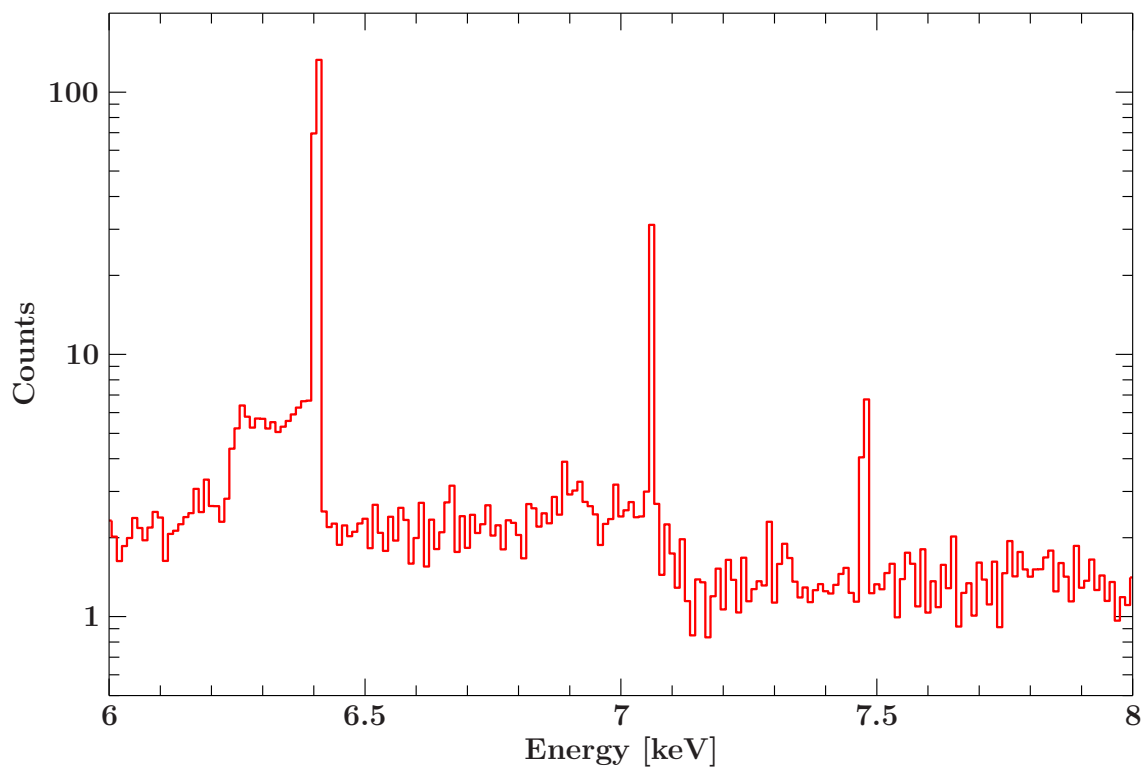The iron band simulated for $\Gamma = 2$ is shown in detail in Figure 35.

Figure 35: The iron band of the reflected spectrum shown in detail.

In the transmitted case the Compton shoulder is nearly covered by the continuum emission and is visible only for a high degree of absorption as seen in Figure 27. In contrast, the pure reflected spectrum exhibits a very pronounced Compton shoulder.

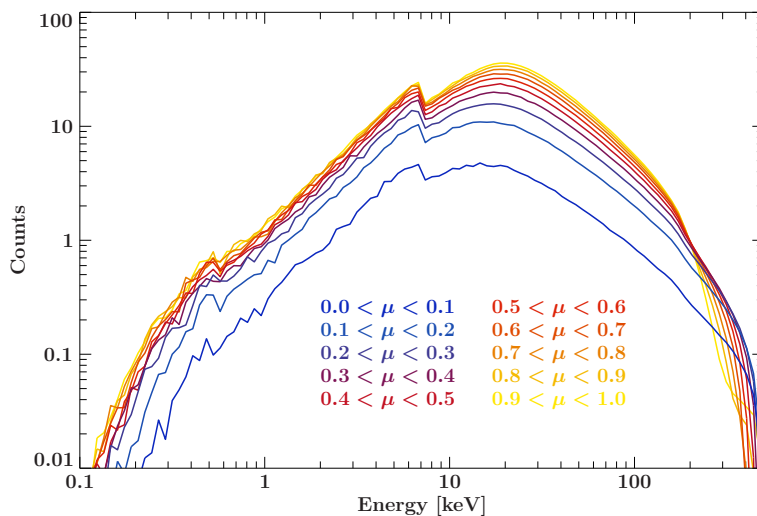### 4.2.2 Angular dependence

Figure 36: Reflected spectrum seen under different inclination angles.

In Figure 36, the reflected spectrum as seen under different viewing angles is plotted. The parameter μ denotes the cosine of the inclination angle. The spectrum is generated for an input

power-law between $0.1 - 500$ keV with photoindex $\Gamma = 2$. As seen, the spectra are not the same for each viewing angle. If the slab is seen nearly edge-on, less photons escape than perpendicular to the slab. For large μ, the hump above ~ 10 keV is more significant and the spectrum decays steeper at high energies. All this features can be understood by considering the pear-shaped Klein-Nishina cross-section (see Fig. 12). Thus, backwards scattering is more probably than a scattering around $90°$. In addition, the photon looses more energy with increasing scattering angle. Assuming an isotropcally illuminated slab, the photons escaping nearly edge-on are scattered on average under a smaller angle ($\sim 90°$) than that ones seen face-on which have scattering angles around $\sim 180°$. Therefore, more photons emerge at large μ and the spectra hardens.
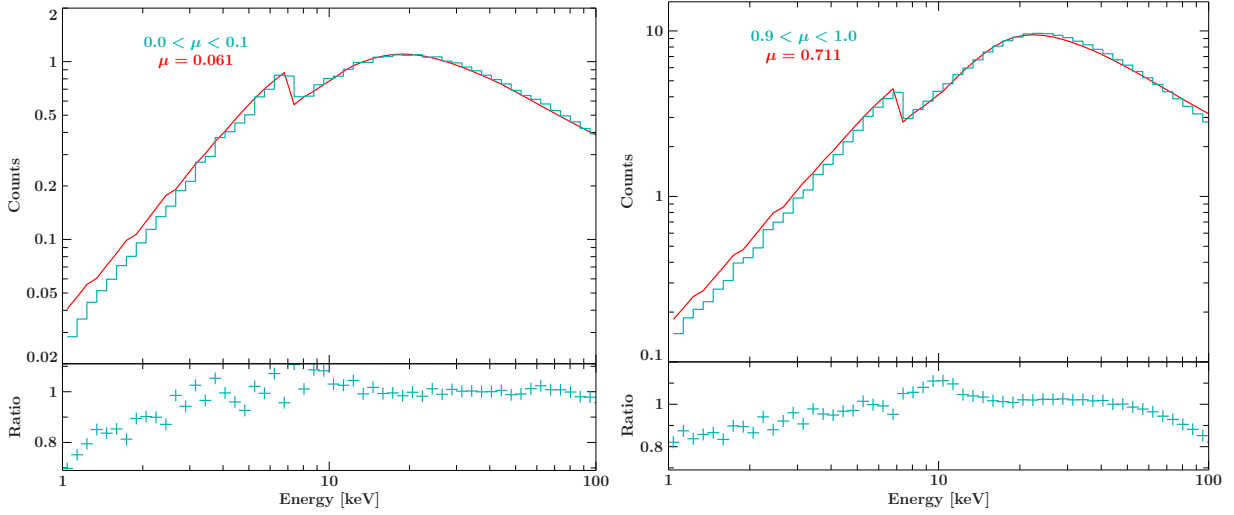

Figure 37: Comparison with the reflection model from Magdziarz & Zdziarski (1995)

For comparison, the angular dependent spectra were fitted with the reflection model from Magdziarz & Zdziarski (1995). The spectra were produced for an incident powerlaw with $\Gamma = 1.7$ expanded from 0.1 to 500 keV and is angular averaged in steps of $\Delta\mu = 0.1$. The fits were performed by fixing the abundances and the powerlawer index since μ is let as free fit parameter. In Figure 37 the results for two different inclination angle are shown. The blue label denotes the cosine range on which the spectrum is averaged and the red one is the best fit value. A feature around 10 keV can be seen in all fits and its significant in the plot on the right side. Whithin this model, the Green's function of Compton reflection is obtained via Monte Carlo calculations. Magdziarz & Zdziarski consider both scattering and photo-absorption, but not over the entire energy range. Photo-absorption is extrapolated with $\propto E^{-3}$ for photon energies above 10 keV. This results in knik around 10 keV as seen in the residues.

Especially for high μ, the fit does not return well the actual values as seen in Figure 38. μ_{mod} denotes the best fit value and μ_{sim} is the actual inclination angle. The respective deviation is plotted as a function of μ_{sim}. Except for $\mu_{sim} = 0.05$, the inclination angle is significantly underestimated for all μ_{sim}. As mentioned above, Magdziarz & Zdziarski do not consider photo-absorption over the full energy range. In addition, different photo-absorption cross-sections and elemental abundances are used in their calculations. The determine where this deviation exactly comes from, additional tests have to be done.
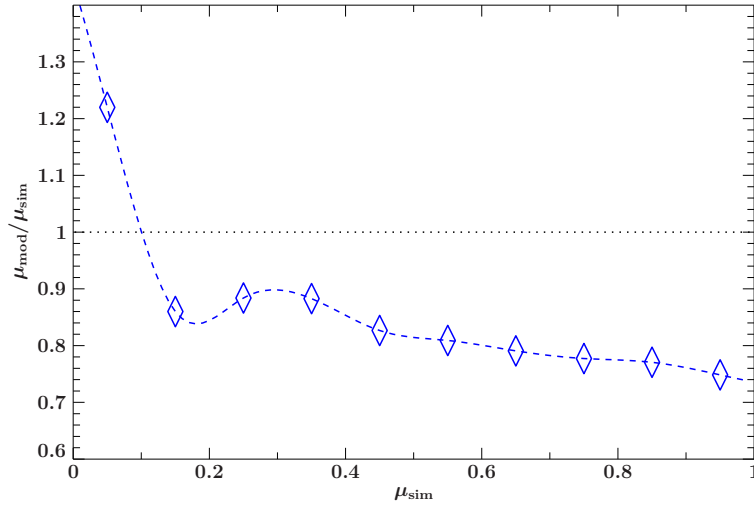
Figure 38: The deviator from the model as a function of μ

5   Shape of iron K_α line and Compton shoulder

Fluorescence lines and other spectral features from low ionized iron have been observed in the spectra of many X-ray sources. Nandra & Pounds (1994) found for example evidence for an iron K_α emission line in the X-Ray spectra of Seyfert galaxies. As the mean energy of the line is around 6.4 keV, it is assumed to originate in near-neutral matter. Iron lines are also observed from X-ray binaries in which the cold dense gas is located very close to the compact object (George & Fabian, 1991). Since the shape and the intensity of the iron line strongly depend on the distribution of the absorbing matter in relation to the source and the quantity of the material, fluorescence lines offer an important diagnostic tool to determine the geometry, elemental abundances and other characteristics of the environment around compact objects.

Iron K_α fluorescence lines emitted in cold and neutral matter consist of the line photons itself forming a narrow core and several Compton shoulders built by line photons that are scattered one or more times (Matt, 2002). The first Compton shoulder (hereinafter CS1) , containing the once-scattered line photons is limited sharply in the lower energy by the maximal energy loss after a single scattering which corresponds to a scattering angle of $\alpha = 180°$ (cf. figure 11). By solving eq. 25 to the photon energy after the event

$$E' = E - \Delta E = \frac{1}{1 + \frac{E}{mc^2}\left(1 - \cos\alpha\right)} \tag{28}$$

the minimal energy a line photon with initial energy 6404.7 eV can reach is calculated to 6248.1 eV.

To give an imagination, how the line features change with changing environment parameters, in figure 39 the iron band is shown in detail for different column densities simulated by using a spherical geometry. As the spectra are calculated for a small energy grid with a bin width of 1 eV, both iron lines the $K_{\alpha I}$ -line at 6.404 keV and the $K_{\alpha II}$ -line at 6.391 keV can be seen separately. In addition to the total spectrum (red curve), the first three Compton shoulders of the iron $K_{\alpha I}$ -line are also plotted.
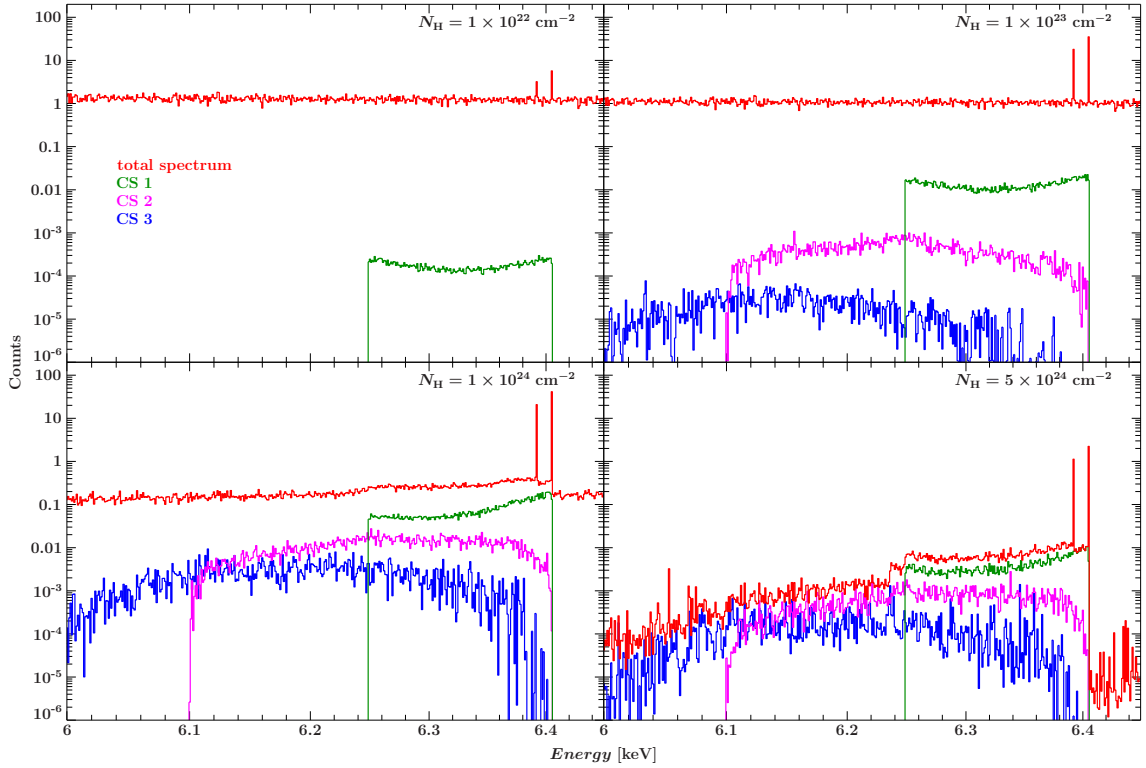
Figure 39: The iron band shown in detail simulated for different column densities.

While for $N_H = 10^{22}$ cm^{-2} only the CS1 is formed because the line photons will be no more scattered than once before they escape. For a higher absorption degree, the second and third CS are growing in comparison to the CS1 as multiple scattering becomes possible. As one can see, the Compton shoulder does not emerge from the continuum until a column density of $\sim 10^{24}$ cm^{-2} and is only significant above that limit. In the last spectrum for $N_H = 5 \times 10^{24}$ cm^{-2}, the lower edge of the CS1 of the K$_{\alpha II}$ -line becomes also visible.

For comparison, the CS1 in the reflection case is shown in figure 40.

To illustrate especially the effect on line photons, the spectra are generated by irradiating the slab isotropically with monochromatic with $E = 6.404$ keV. It is immediately apparent that the CS1 shifts to smaller energies for a larger inclination angle $\mu = \cos(\alpha)$. That is what we expect as a photon that escapes almost perpendicular to the slab is on average back-scattered at a greater angle than it is the case for small μ and the energy loss increases with increasing scattering angle. The small peak in the CS1 for $\mu = 0.95$ (red curve) comes from photons that have beam almost parallel to the slab and then were scattered forwards.

In the following, the equivalent width of the NC of the iron K$_{\alpha I}$ -line, the centroid energy of the first CS as well as the relative amount of photons in CS1 to the number of line photons are calculated for both transmitted and reflected spectra. In the former case, the values are computed for column densities between $1 \times 10^{22} - 5 \times 10^{24}$ cm^{-2}. For the reflected spectra, each value is determined as a function of the inclination angle $\mu = \cos(\alpha)$, where α is the angle between the surfaces normal and the line of sight. To allow comparison with the results from Matt (2002), the elemental abundances from Morrison & McCammon (1983) are adopted for these simulations. To
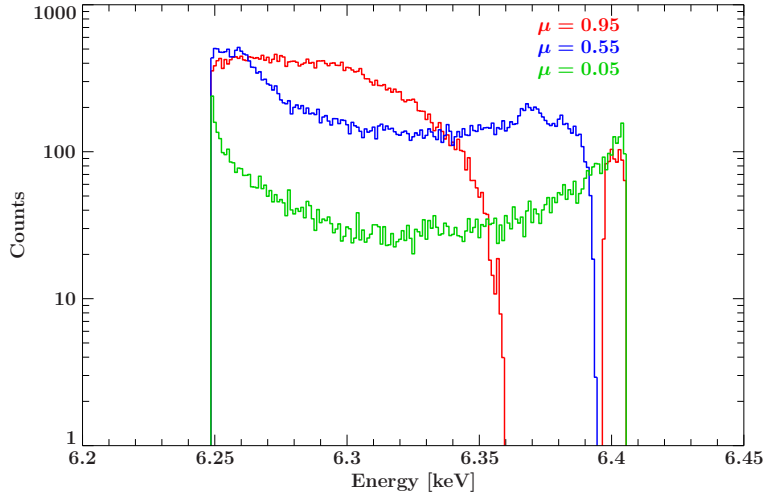
Figure 40: The first Compton shoulder in the reflection case for different inclination angle μ

show the dependence of the line parameters on the iron abundance A_{Fe}, the values are additionally calculated for the half and the twice amount of iron with respect to the cosmic value.

5.1 Equivalent width

The equivalent width (hereinafter EW) of the NC is a measure of the area of a spectral line on a plot of intensity versus energy in relation to the continuum. It is calculated by forming a rectangle with the same area as the line is taking and the same height as the continuum emission (cf. fig. 41). The width of the resulting rectangle is the EW. To determine which photon is a iron $K_{\alpha I}$ -line photon and which belongs to the continuum, the line photons generated are marked in the simulation and counted separately. In this way, the number of line photons N_L and that of the continuum N_C in each energy bin is clear. The EW is than given by

$$EW = \frac{N_L \times \Delta E}{N_C}$$
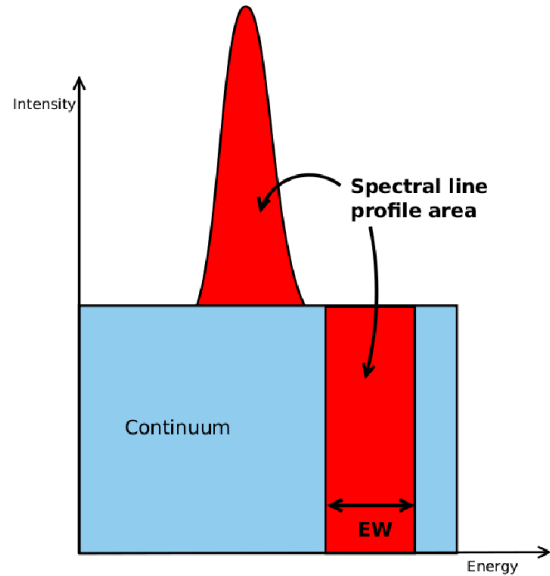
where ΔE is the bin width.

Figure 41: Definition of the equivalent width of a spectral line

Transmitted spectra   In figure 42 on the left plot, the results for three different iron abundances are shown . On the right one, the curve for $A_{Fe} = 1$ is compared with the results from Matt (2002).
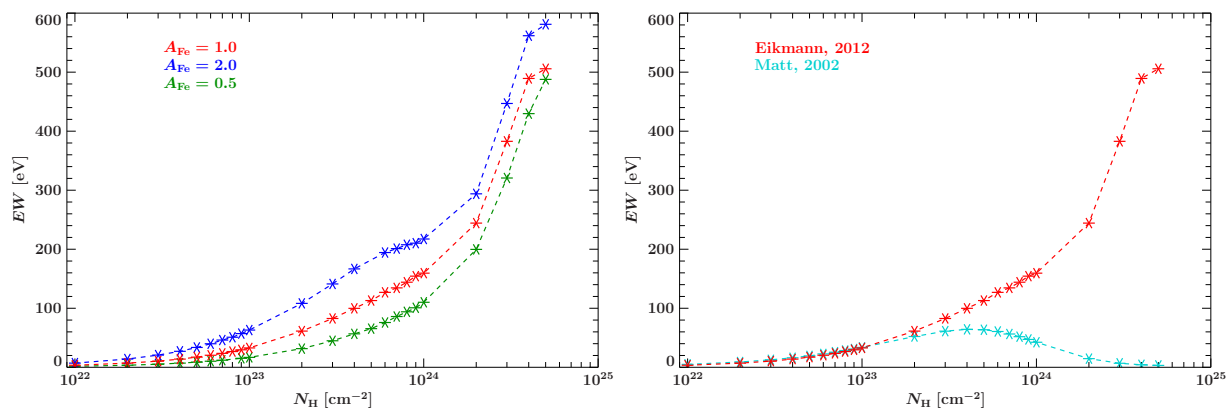
58

Figure 42: Equivalent width of the $K_{\alpha I}$ -line for transmitted spectra.

As one can see on the left plot, the EW of the iron $K_{\alpha I}$ -line increases with the column density and the increase is significantly larger for $N_H \gtrsim 10^{24}$ cm^{-2}. At a Thomson optical depth $\tau_T > 1$ corresponding to a column density greater than 1.5×10^{24} cm^{-2} the size of the medium exceeds the mean distance a photon can travel without a check (see eqs. 11 and 23) and multiple scattering becomes important. This has the consequence that the continuum is dramatically more absorbed for $\tau_T > 1$ resulting in an increasing EW.
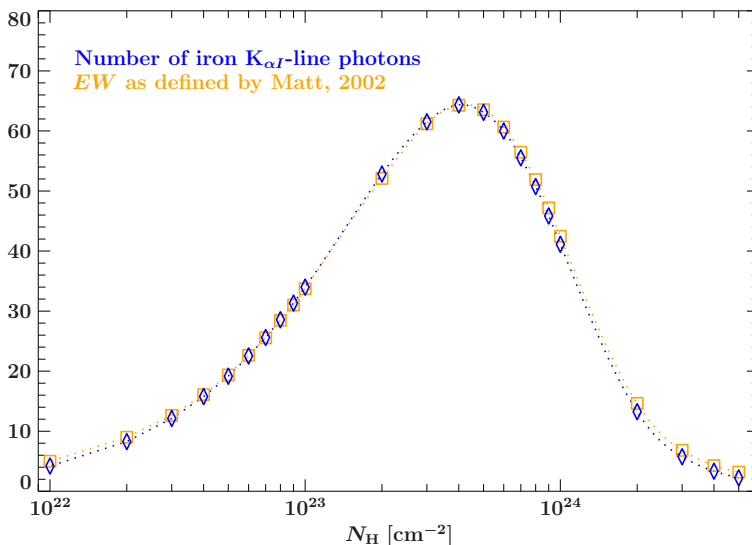

Figure 43: Number of escaping iron $K_{\alpha I}$ -line photons for $A_{Fe} = 1$ versus column density (red curve). The EW as it is defined by Matt (2002) is also plotted.

The number of line photons N_L also decreases for $N_H \gtrsim 4 \times 10^{23}$ cm^{-2} as the blue curve of figure 43 shows, but not in this dimension as the continuum does. The reason for this is that the continuum is continuously absorbed on the whole way from the center to the edge of the cloud. The line photons in contrast can be regenerated via fluorescence in each place of the medium. Therefore the line is also visible for highly obscured sources where the escaping line photons mainly come from the mediums outer borders. From $N_H \sim 10^{24}$ cm^{-2} also the dependence of the iron abundance A_{Fe} changes: Below this limit, the EW grows linear with N_H as it is also found by Matt. Above $\sim 10^{24}$ cm^{-2}, this is no longer valid.

The results are consistent with those from Matt (2002) only for $N_H \lesssim 10^{23}$ cm^{-2} as the direct comparison for $A_{Fe} = 1$ shows on the right plot of fig. 42. To avoid a covering of the iron band by down-scattered photons, Matt uses in his calculations only primary photons with a minimal energy around the iron K-edge energy, but the exact energy remains unclear as well as on which continuum the EW is referred to. In addition to the number of iron $K_{\alpha I}$-line photons, the values from Matt are plotted again in fig. 43 (orange curve). The agreement with the data for N_L gives evidence for an unusual definition of the EW used by Matt.
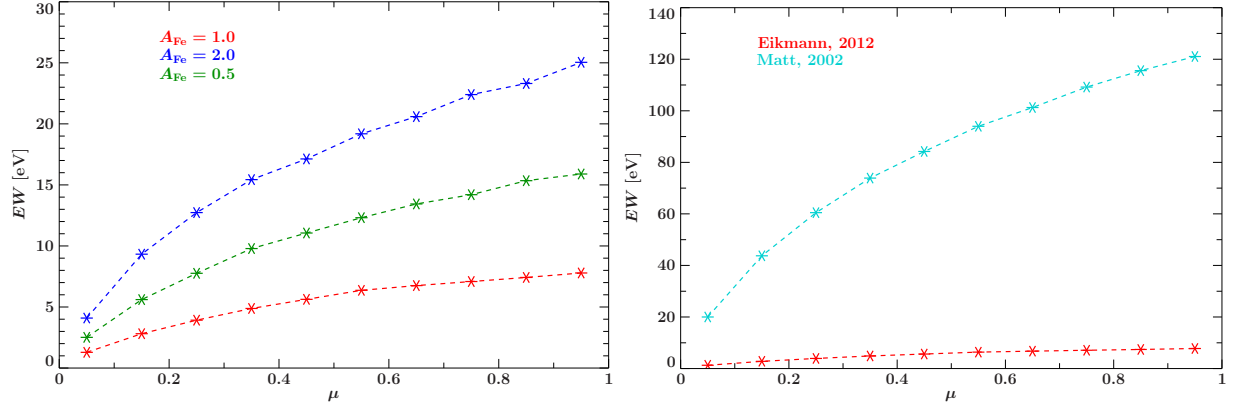

Figure 44: Equivalent width of the $K_{\alpha I}$-line for reflected spectra.

Reflected spectra As a reflected X-ray spectrum is usually observed together with the primary radiation of the X-ray source (see fig. 34), the EW is calculated with respect to the input photon spectrum. In figure 44, both the results for different iron abundances as a function of μ and the comparison with Matt are shown. The EW of the NC increases with μ as it is also found by Matt (2002). As it can be seen in fig. 12 the Compton scattering cross-section has a local minimum at a scattering angle of 90° meaning that more photons are back scattered than sidewards. For this reason less photons are available for fluorescence perpendicular to the beam direction of the incident photons. In this way, the EW grows with μ although a line photon is emitted isotropically. The dependence on the iron abundances is again almost linear.

The values for the EW are significantly smaller than those presented by Matt as the comparison on the right plot shows. Again, it is unclear on which continuum Matt refers to as well as the exact definition of the EW he used.

5.2   Centroid energy of the first Compton shoulder

The shape of the CS1 change with changing column density as it is shown in Figure 39. For low column density, the CS1 is approximately symmetric while its low energetic edge decreases with respect to the high energetic one for a higher absorption degree. This asymmetry can be expressed in the centroid energy E_C of the CS1 which is defined as

$$E_C = \frac{\int_{E_{Rec}}^{E_L} E N(E) \mathrm{d}E}{\int_{E_{Rec}}^{E_L} N(E) \mathrm{d}E} \tag{29}$$

60

where E_L is the iron $K_{\alpha I}$-line energy and E_{Rec} the minimal energy a line photon can reach after a single scattering (see eq. 28) . To identify those photons which actually belongs to the CS1 and not to the continuum, the line photons those escape after one scattering are binned separately.

Transmitted spectra In figure 45, the results are shown together with the values calculated by Matt. The E_C increases up to a column density of $N_H \approx 1 \times 10^{24}$ cm^{-2} and than decreases again. The rise comes from the fact that Compton scattering is not isotropically but forward-scattering is preferred still at energies around the iron line. As this means a lower energy loss than backward-scattering, more photons can be found in the right edge of the CS1. In addition, the cross-section for scattering grows with decreasing photon energy and for this reason, more photons are scattered down from the left edge of the CS1. The following decrease is because multiple scattering becomes important in this regime and a large part of the CS1 photons are down scattered. The results are nearly independent of the iron abundance.

Matt found a similar behavior but the whole curve is shifted to a smaller E_C. This is because Matt has been used as line energy $E_L = 6.4$ keV rather than the more exact value $E_L = 6404.7$ eV as it is done in this calculations. This results in a shift of E_C to lower energies.
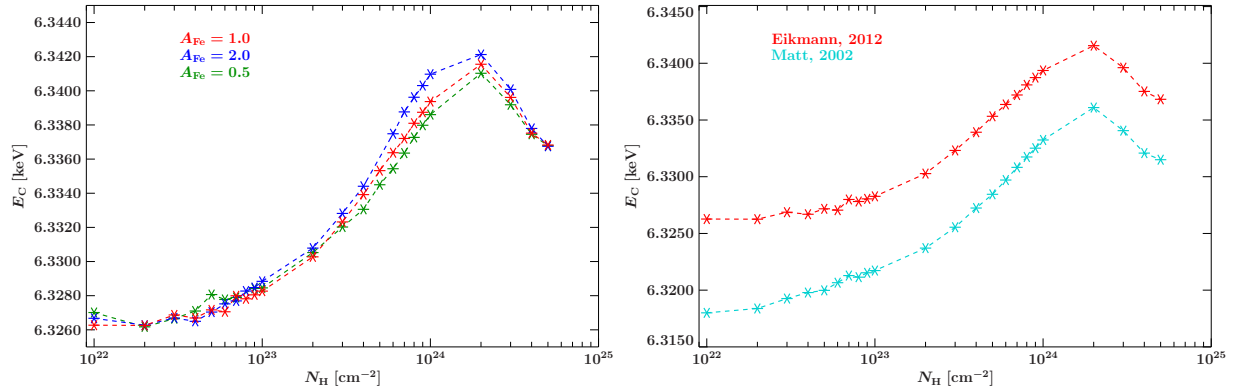

Figure 45: Centroid energy of the first Compton shoulder for the transmitted case

Reflected spectra The E_C of the CS1 decreases for increasing μ as the plot in figure 46 shows. By considering the shape of the reflected CS1 on figure 44 and the related declarations this is exactly what we expect. Again, the iron abundance does not affect much the results. As it was for the transmitted case, Matt found also lower values for the reflected CS due to he assumed a lower line energy.

5.3 Ratio between the intensity of the line and the first Compton shoulder

Finally, the ratio between the total amount of photons in the CS1 (N_{CS1}) to that in the NC is calculated by computing
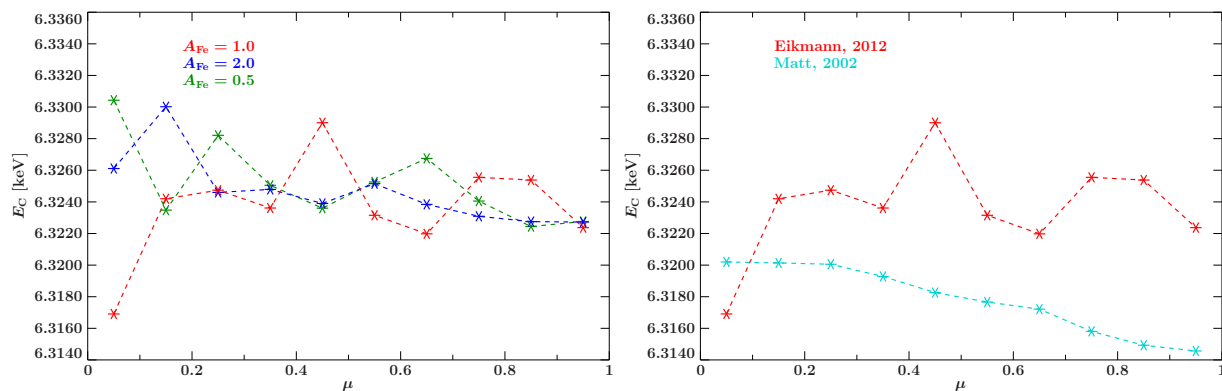
$$f = \frac{N_{CS1}}{N_L}.$$

61

Figure 46: Centroid energy of the reflected Compton shoulder

Transmitted spectra As it can be seen in figure 47, f increases with the column density and has a maximum around $N_H \approx 2 \times 10^{24}$ cm^{-2}. Up to this value, line photons are continuously scattered down in the CS1 and remaining there as multiple scattering is rare at this absorption degree. Above this limit, the photons are scattered in average more than once and f decreases again. The dependence on the iron abundances is almost negligible.

The results agree well with those from Matt considering that he assumed a slightly different energy range for the CS1 leading to a shift of the whole curve.
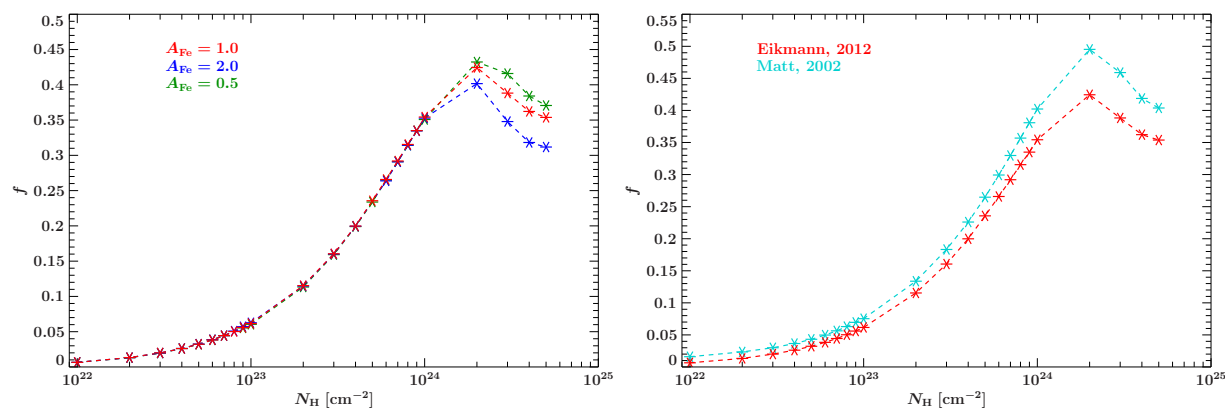

Figure 47: Ratio of photons in the CS1 to that in the NC for transmission

Reflected spectra As more line photons are emitted perpendicular to the slab, f increases with increasing μ (see fig. 48). The ratio f is naturally slightly smaller for higher iron abundances. The values agree again well with those found by Matt. He additionally noticed, that for the same iron abundance f is lower in reflected than in transmitted spectra provided that the column densities is a few times of 10^{23} cm^{-2}. Line photons originates from the outer layers of the absorbing medium especially for high column densities. In the slab geometry, the effective surface in the line of sight is larger as in a spherical cloud and therefore more line photons can escape than in the transmitted case.
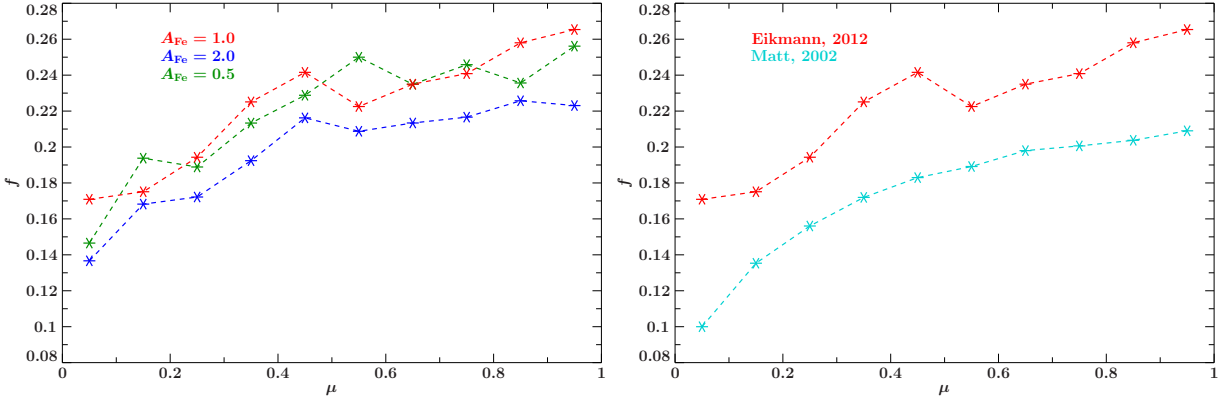
Figure 48: Ratio of photons in the CS1 to that in the NC for reflection

6   Summary and Outlook

The spectra of almost all astrophysical X-ray sources are modified by absorption or reflection from the interstellar medium. To understand the spectra of the sources, the knownledge of this modification is from crucial importance. In addition, the altered spectrum contains information about the interstellar medium itself and provides an important diagnostic tool to explore the environement of compact objects.

The parameters of interest like the degree of absorption in transmitted spectra or the viewing angle in the reflected case as well as the elemental abundances are usually determined by comparing the observational data with existing models. The range of validity strongly depends on the considered physical processes. This shows the comparison of the Monte Carlo calculated spectra with the absorption model tbabs and the reflection model from Magdziarz & Zdziarski.

A set of parameters that describe the intensity and shape of the important iron K_α-line is also presented in this thesis. The caculated values, especially the equivalent width, differs from prior results done by Matt. The values presented here may descibed observational data better as discussed in chapter 5.

The next step would be to provide this simulation also as a fit model and to compare it with the spectra from natural sources. Until now, there is no absorption model available which fully include both Compton scattering and photo-absorption. A model of line emission doesn't exists either and therefore each single fluoresence line has to be modeled separately in the observational spectra, usually by fitting a Gaussian profile. As the lines exhibits a pronounced Compton shoulder for high column densities or in the reflected case, this is not always true. Within the Monte Carlo simulation, the exact shape of the fluoresence lines can be calculated together with the corresponding Compton shoulder for each set of input parameters.

References

Weigert, A., Wendker, H., & Wisotzki, L. 2005, Astronomie und Astrophysik (Weihnheim: WILEY-VCH)

Arnaud, K. A. 1996, in Astronomical Society of the Pacific Conference Series, Vol. 101, Astronomical Data Analysis Software and Systems V, ed. G. H. Jacoby & J. Barnes, 17

Bambynek, W., Crasemann, B., Fink, R. W., et al. 1972, Reviews of Modern Physics, 44, 716

Caflisch, R. E. 1998, Acta Numerica, 7, 1

Champeaux, J.-P., Bizau, J.-M., Cubaynes, D., et al. 2003, ApJS, 148, 583

Chandrasekhar, S. 1931, ApJ, 74, 81

Compton, A. H. 1923, Physical Review, 21, 483

Deak, I. 1990, Random Number Generators and Simulation (Mathematical Methods of Operations Research, 4, Budapest: Akadamiai Kiado)

Demtröder, W. 2006, Atoms, Molecules and Photons (Springer)

Downham, D. Y., & Roberts, F. D. K. 1967, 10, 74

Fabian, A. C. 2006, in ESA Special Publication, Vol. 604, The X-ray Universe 2005, ed. A. Wilson, 463

Frank, J., King, A., & Raine, D. 2002, Accretion Power in Astrophysics, 3rd edn. (Cambridge University Press), 400

Friedman, H., Lichtman, S. W., & Byram, E. T. 1951, Physical Review, 83, 1025

Fürst, F., Kreykenbohm, I., Pottschmidt, K., et al. 2010, AAP, 519, A37

George, I. M., & Fabian, A. C. 1991, MNRAS, 249, 352

Giacconi, R., Gursky, H., Paolini, F. R., & Rossi, B. B. 1962, Physical Review Letters, 9, 439

Glasserman, P. 2003, Monte Carlo Methods in Financial Engineering (Stochastic Modelling and Applied Probability) (v. 53), 1st edn. (Springer)

Haberl, F., & White, N. E. 1990, ApJ, 361, 225

Hansen-Ruiz, C. S., & van Leeuwen, F. 1997, in ESA Special Publication, Vol. 402, Hipparcos - Venice '97, ed. R. M. Bonnet, E. Høg, P. L. Bernacca, L. Emiliani, A. Blaauw, C. Turon, J. Kovalevsky, L. Lindegren, H. Hassan, M. Bouffard, B. Strim, D. Heger, M. A. C. Perryman, & L. Woltjer, 295–298

Hertzsprung, E. 1911, Publikationen des Astrophysikalischen Observatoriums zu Potsdam, 63

Iwasawa, K., Koyama, K., Awaki, H., et al. 1993, ApJ, 409, 155

Jansky, K. G. 1933, Nature, 132, 66

Kaastra, J. S., & Mewe, R. 1993, in UV and X-ray Spectroscopy of Laboratory and Astrophysical Plasmas, ed. E. H. Silver & S. M. Kahn, 134

Kalos, M. H., & Whitlock, P. A. 2008, Monte Carlo methods (Weinheim: WILEY-VCH), XII, 203 S.

Karzas, W. J., & Latter, R. 1961, ApJS, 6, 167

Kippenhahn, R., & Weigert, A. 1990, Stellar Structure and Evolution (Berlin: Springer-Verlag)

Kreykenbohm, I. 2004, dissertation, Institut fur Astronomie und Astrophysik, Eberhard-Karls-Universität Tübingen

Lightman, A. P., & White, T. R. 1988, ApJ, 335, 57

Lindegren, L. 1992, Status and early results of the HIPPARCOS astrometry project, Tech. rep.

Magdziarz, P., & Zdziarski, A. A. 1995, MNRAS, 273, 837

Maiolino, R., Salvati, M., Bassani, L., et al. 1998, AAP, 338, 781

Matt, G. 2002, MNRAS, 337, 147

Matt, G., Perola, G. C., & Piro, L. 1991, AAP, 247, 25

Matt, G., Pompilio, F., & La Franca, F. 1999, New Astronomy, 4, 191

McKee, C. F., & Ostriker, E. C. 2007, Annual Review of Astronomy and Astrophysics, 45, 565

Metropolis, N. 1987, Los Alamos Science Special Issue, 125

Mooney, C. Z. 1997, Monte Carlo Simulation, Sage university paper series on quantitative applications in the social sciences, 07-116 (Beverly Hills, CA: Sage Publications)

Morrison, R., & McCammon, D. 1983, ApJ, 270, 119

Nandra, K., & Pounds, K. A. 1994, MNRAS, 268, 405

Nekovar, S. 2012, Project, Friedrich-Alexander-University of Erlangen-Nürnberg

Odaka, H., Aharonian, F., Watanabe, S., et al. 2011a, ApJ, 740, 103

Odaka, H., Tanaka, Y., Watanabe, S., et al. 2011b, in The X-ray Universe 2011, ed. J.-U. Ness & M. Ehle, 115

Porter, J. M., & Rivinius, T. 2003, 115, 1153

Pozdnyakov, L. A., Sobol, I. M., & Syunyaev, R. A. 1983, Astrophysics and Space Physics Reviews, 2, 189

Rolfs, C. E., & Rodney, W. S. 1988, Cauldrons in the Cosmos ("The University of Chicago Press")

Rosenberg, H. 1911, Astronomische Nachrichten, 189, 365

Russell, H. N. 1914, Popular Astronomy, 22, 275

Rybicki, G. B., & Lightman, A. P. 1986, Radiative Processes in Astrophysics

Salaris, M., & Cassisi, S. 2005, Evolution of stars and stellar populations (Chichester: WILEY-VCH)

Salpeter, E. E. 1955, Vistas in Astronomy, 1, 283

—. 1964, ApJ, 140, 796

Sato, N., Hayakawa, S., Nagase, F., et al. 1986, PASJ, 38, 731

Srinivasan, G. 1997, in Stellar Remnants, ed. S. D. Kawaler, I. Novikov, & G. Srinivasan, 97–235

Trümper, J., & Murdin, P. 2000, X-Ray Astronomy, ed. Murdin, P.

Ulam, S. M. 1976, Adventures of a mathematician (New York, NY: Schribner's)

van den Heuvel, E. P. J. 2011, Bulletin of the Astronomical Society of India, 39, 1

Verner, D. A., & Yakovlev, D. G. 1995, AAPS, 109, 125

Weidemann, V., Jordan, S., Iben, Jr., I., & Casertano, S. 1992, ApJ, 104, 1876

White, N. E., Nagase, F., & Parmar, A. N. 1995, X-ray Binaries, 1

Wichmann, B. A., & Hill, I. D. 1982, 31, 188

Wilms, J. 1996, Diploma thesis, Institut fur Astronomie und Astrophysik, Abt. Astronomie, Eberhard-Karls-Universität Tübingen

Wilms, J. 2002

Wilms, J., Allen, A., & McCray, R. 2000, ApJ, 542, 914

Zel'Dovich, Y. B. 1964, Soviet Physics Doklady, 9, 195

Zuckerman, B., & Palmer, P. 1974, Annual Review of Astronomy and Astrophysics, 12, 279

Erklärung

Ich versichere, dass ich diese Arbeit selbstständig verfasst und keine anderen als die angegebenen Quellen und Hilfsmittel benutzt habe.

Bamberg, den 31.05.2012   . . . .